Vol. 1, No. 1 (2024)

Open Plasma Science

Regular article

Impurity Parallel Velocity Gradient instability

Jeanne Bourgeois[1,2], Maxime Lesur[*,3,4], Guillermo Cuerva Lazaro[3], and Yusuke Kosuga[5,6]

[1]Ecole Polytechnique, Institut Polytechnique de Paris, 91128 Palaiseau, France
[2]Interdisciplinary Graduate School of Engineering Sciences, Kyushu University, Fukuoka, Japan
[3]Université de Lorraine, CNRS, Institut Jean Lamour, UMR 7198, F-54000 Nancy, France
[4]Institut Universitaire de France (IUF), Paris, France
[5]Research Institute for Applied Mechanics, Kyushu University, Kasuga, Fukuoka 816-8580, Japan
[6]Research Center for Plasma Turbulence, Kyushu University, Kasuga, Fukuoka 816-8580, Japan

History
Received May 20, 2024
Revised August 16, 2024
Accepted October 05, 2024
Published October 29, 2024

Identifiers
DOI 10.46298/ops.13628
HAL -
ArXiv 2405.08472

Supplementary Material
-

Abstract

In magnetized plasmas, a radial gradient of parallel velocity, where parallel refers to the direction of magnetic field, can destabilise an electrostatic mode called Parallel Velocity Gradient (PVG). The theory of PVG has been mainly developed assuming a single species of ions. Here, the role of impurities is investigated based on a linear, local analysis, in a homogeneous, constant magnetic field. To further simplify the analysis, the plasma is assumed to contain only two ion species — main ions and one impurity species — while our methodology can be straightforwardly extended to more species. In the cold-ion limit, retaining polarization drift for both main ions and impurity ions, and assuming Boltzmann electrons, the system is described by 4 fluid equations closed by quasi-neutrality. The linearized equations can be reduced to 2 coupled equations: one for the electric potential, and one for the effective parallel velocity fluctuations, which is a linear combination of main ion and impurity parallel velocity fluctuations. This reduced system can be understood as a generalisation of the Hasegawa-Mima model. With finite radial gradient of impurity parallel flow, the linear dispersion relation then describes a new instability: the impurity-modified PVG (i-PVG). Instability condition is described in terms of either the main ion flow shear, or equivalently, an effective flow shear, which combines main ion and impurity flow shears. Impurities can have a stabilising or destabilising role, depending on the parameters, and in particular the direction of main flow shear against impurity flow shear. Assuming a reasonable value of perpendicular wavenumber, the maximum growth rate is estimated, depending on impurity mass, charge, and concentration.

Keywords— Magnetized plasma, Parallel Velocity Gradient instability, Impurity

* Corresponding author: maxime.lesur@univ-lorraine.fr

Cite as: Bourgeois *et al.*, Impurity Parallel Velocity Gradient instability, *Open Plasma Science* 1, 1 (2024), doi: 10.46298/ops.13628

Contents

1 Introduction

In magnetized plasmas, the Parallel Velocity Gradient (PVG), or Parallel Velocity Shear (PVS) is a type of Kelvin-Helmholtz fluid instability driven by a radial gradient of parallel (to magnetic field) plasma flow. It is sometimes referred to as D'Angelo instability, since D'Angelo investigated a simplified version (simplified by a radial WKB approximation) for a low-temperature plasma in a uniform magnetic field [D'A65]. The D'Angelo instability was then observed in basic plasma experiments [DG66, KTH03].

In toroidal magnetic confinement fusion devices, magnetic shear is stabilising [CRL73]. However, theory indicates that PVG-driven turbulence may be found in the vicinity of transport barriers [McC02, GSG+02], in the SOL [DHG+92], in the presence of strong parallel beam injection, and more readily in spherical tokamaks [CBKW12, WER+15]. Even in cases where PVGs are weak, they can have important impact by coupling with Ion-Temperature-Gradient (ITG) turbulence. Theory predicted subcritical ITG-PVG turbulence [NCL10, BPH+11, SHC12, HSC+12], which is consistent with measurements (by Beam Emission Spectroscopy) on MAST [FDG+12]. Strong experimental hints, from fluctuation level and isotropy of correlation length, indicate a significant contribution of PVG-driven turbulence in the edge of the CT-6B tokamak plasma [WWY+98]. The universality of PVGs in tokamaks remains an open issue.

Parallel flows are also expected to play major roles in linear magnetized plasma devices, such as PANTA (Plasma Assembly for Nonlinear Turbulence Analysis, formerly LMD), where an uphill, near-axis, axial particle flux [KIK+16] has been measured to be consistent with PVG/drift-waves coupling [IKK+16], with a regime transition in quantitative agreement with the theoretical linear instability threshold [KII15].

Magnetic confinement fusion plasmas are often contaminated by ion species other than hydrogen isotopes, which are then called as impurities. These can include helium, nitrogen, neon, argon, beryllium, carbon, and tungsten. Linear magnetized plasma experiments can also include impurities. In particular, a new linear device, called SPEKTRE (Sheath, Plasma Edge & Kinetic Turbulence Radiofrequency Experiment) [BGH+23] and currently under construction, is partly designed to inject various impurities in a controlled manner and investigate their impact and their dynamics.

Our objective here is to investigate the instability driven by a radial shear of the parallel flows of multiple species, which we refer to as impurity-modified PVG (i-PVG). We consider experimental conditions that are relevant to linear plasma experiments with cylindrical geometry such as PANTA and SPEKTRE, and are insightful approximations of tokamak's edge plasma, where the PVG instability is of its most significance. Our local, linearized model can be understood as a modified Hasegawa-Mima model including equilibrium and perturbed parallel velocities of both main ions and impurities.

In the case of slab geometry with weak magnetic shear, Guo obtained from gyrokinetic equations a linear dispersion relation for PVG with impurities, showing the stabilization of the PVG instability by the presence of impurities and by the increase of electron density gradient [GWZ19]. Here we adopt a fluid approach, and investigate how the i-PVG threshold, frequency and growth rate depend on parameters such as impurity charge, mass, concentration and parallel flow shear. We further assume a cold-ion limit to provide more clear analysis of the i-PVG. Our fluid approach is supported by this cold ion assumption, plus by the fact that our study focuses on the linear growth of the instabilities and ignores the damped states, so that kinetic effects such as Landau damping can be neglected. Compared to Guo's previous work, our approach provides a more flexible analysis in terms of parameter scan for independent ion and impurity flow shears, and demonstrates that the presence of impurity can be either stabilizing or destabilizing for PVG. The relationship between linear properties and plasma parameters turns out to be somewhat complex, with several non-monotonous dependencies.

2 Model

The model is based on a local approximation in a Cartesian basis ($\hat{\boldsymbol{e_x}}$, $\hat{\boldsymbol{e_y}}$, $\hat{\boldsymbol{e_z}}$). The magnetic field is assumed homogeneous and constant, $\boldsymbol{B} = B\hat{\boldsymbol{e_z}}$. Hereafter, the parallel and perpendicular subscripts ($\parallel$ and $\perp$) refer to the direction of the magnetic field $\hat{\boldsymbol{e_z}}$ and the perpendicular plane ($\hat{\boldsymbol{e_x}}$, $\hat{\boldsymbol{e_y}}$). For each species s, both equilibrium density gradient and equilibrium parallel velocity gradient are assumed constant and in the x direction:

$$\boldsymbol{\nabla} n_{s,0} = \frac{n_{s,0}}{L_{n,s}} \hat{\boldsymbol{e_x}} \tag{1}$$

$$\boldsymbol{\nabla} u_{\parallel,s,0} = \frac{u_{\parallel,s,0}}{L_{u,s}} \hat{\boldsymbol{e_x}} \tag{2}$$

where $L_{n,s}$ and $L_{u,s}$ are the density gradient length and parallel velocity gradient length.

We assume for simplicity that the plasma contains only electrons ($s = e$) and two ion species (one main ion species $s = i$, and one impurity species $s = z$), although the model can be straightforwardly generalized to more species. For each species, mass is noted m_s, and charge is noted $q_s = Z_s e$, where e is the elementary charge ($Z_e = -1$ and, for simplicity, we assume that the main ions satisfy $Z_i = 1$).

We adopt the cold ion limit, setting for the wave number an approximate maximum limit $\sqrt{T_e/T_s}/\rho_s$, with $s = i$ and z, and $\rho_{c,s}$ being the Larmor radius of species s. The perpendicular motion of ions (both main ions and impurity ions) is dominated by $E \times B$ drift,

$$\boldsymbol{u_E} = \frac{\boldsymbol{E} \times \boldsymbol{B}}{B^2} \tag{3}$$

and polarization drift,

$$\boldsymbol{u_{p,s}} = \frac{1}{\omega_{c,s} B} \boldsymbol{B} \times \frac{\mathrm{d}\boldsymbol{u_E}}{\mathrm{d}t} = \frac{1}{\omega_{c,s} B} \frac{\mathrm{d}\boldsymbol{E}_\perp}{\mathrm{d}t} \tag{4}$$

This is valid up to first order in terms of the ratio between wave frequency and cyclotron frequency, $\omega/\omega_{c,s}$. Here, as verified a posteriori, $\omega/\omega_{c,i}$ remains as small as a few percent. However, since $\omega_{c,z}/\omega_{c,i} = Z_z m_i/m_z$,

the model requires heavy impurities to be sufficiently ionized (unless these impurities are in high enough concentration to bring ω down to small enough values).

These assumptions yield a system of four fluid equations. Namely, for each of $s = i$ and z, the density equation writes as

$$\frac{\partial n_s}{\partial t} + \boldsymbol{\nabla}_\perp \cdot [n_s(\boldsymbol{u_E} + \boldsymbol{u_{p,s}})] + \nabla_\parallel (n_s u_{\parallel,s}) = 0 \tag{5}$$

and the parallel flow equation writes as

$$\frac{\partial u_{\parallel,s}}{\partial t} + (\boldsymbol{u_E} + \boldsymbol{u_{p,s}}) \cdot \boldsymbol{\nabla}_\perp u_{\parallel,s} + u_{\parallel,s} \nabla_\parallel u_{\parallel,s} = -\frac{q_s}{m_s} \nabla_\parallel \phi \tag{6}$$

Assuming that electron density n_e responds to electrostatic fluctuations ϕ according to a Boltzmann distribution, the system of equations is closed by quasi-neutrality,

$$\sum_{s \neq e} Z_s n_s = n_e = n_0 \exp\left(\frac{e\phi}{T_e}\right) \tag{7}$$

where T_e is the temperature.

3 Linear analysis

To obtain the linear dispersion relation, densities and parallel velocities are split into equilibrium and fluctuation parts, $n_s = n_{s,0} + \tilde{n_s}$ and $u_{\parallel,s} = u_{\parallel,s0} + \tilde{u}_{\parallel,s}$. Then, Eqs. (5)-(7) are linearized,

$$\frac{\partial \tilde{n_s}}{\partial t} + \boldsymbol{u_E} \cdot \boldsymbol{\nabla}_\perp n_{s,0} + n_{s,0} \boldsymbol{\nabla}_\perp \cdot \boldsymbol{u_{p,s}} + n_{s0} \nabla_\parallel \tilde{u}_{\parallel,s} = 0 \tag{8}$$

$$\partial_t \tilde{u}_{\parallel,s} + \boldsymbol{u_E} \cdot \boldsymbol{\nabla}_\perp u_{\parallel,s,0} = -\frac{q_s}{m_s} \nabla_\parallel \phi \tag{9}$$

$$\sum_{s \neq e} Z_s \tilde{n_s} = n_{e,0} \frac{e\phi}{T_e} \tag{10}$$

Here we used the assumption of homogeneous magnetic field to remove the term in $\boldsymbol{\nabla} \cdot \boldsymbol{u_E}$. In addition, we neglected four terms which remain small for typical plasma parameters:

1. The term $\boldsymbol{u_{p,s}} \cdot \boldsymbol{\nabla}_\perp n_{s,0}$ is of order $\omega/\omega_{c,s}$ compared to $\boldsymbol{u_E} \cdot \boldsymbol{\nabla}_\perp n_{s,0}$. Note that, compared to $n_{s,0} \boldsymbol{\nabla}_\perp \cdot \boldsymbol{u_{p,s}}$, it is of order $k_x/(k_\perp^2 L_n)$, which, as verified a posteriori, remains much smaller than unity as long as $\rho_{c,i}/L_n \ll 1$.

2. Similarly, the term $\boldsymbol{u_{p,s}} \cdot \boldsymbol{\nabla}_\perp u_{\parallel,s,0}$ is of order $\omega/\omega_{c,s}$ compared to $\boldsymbol{u_E} \cdot \boldsymbol{\nabla}_\perp u_{\parallel,s,0}$.

3. The term $u_{\parallel,s0} \nabla_\parallel \tilde{n_s}$, compared to $\partial \tilde{n_s}/\partial t$, is of order $k_\parallel u_{\parallel,s0}/\omega$, which must remain small to avoid strong Landau damping. Note that, compared to $\boldsymbol{u_E} \cdot \boldsymbol{\nabla}_\perp n_{s,0}$, it is of order $(T_i/T_e) M_s^2$, where $M_s = u_{\parallel,s0}/v_{T,i}$ is the Mach number for species s. To obtain the latter ordering, we substituted $k_\parallel$ by $\frac{\overline{\nabla u_\parallel}}{2\overline{\omega_c}} k_y$ (which provides the strongest instability, cf Eq. (20) for justification), and assumed that for each species, density and parallel gradient lengths are comparable. Extension of this theory for plasmas where the condition $M_s^2 \ll T_e/T_i$ is not satisfied, is left for future work, as accounting for the term $u_{\parallel,s0} \nabla_\parallel \tilde{n_s}$ expands a parameter space that is already very large.

4. Similarly, the term $u_{\parallel,s0}\nabla_\parallel \tilde{u}_{\parallel,s}$, compared to $\partial\tilde{u}_{\parallel,s}/\partial t$, is of order $k_\parallel u_{\parallel,s0}/\omega$.

A linear combination reduces the system Eqs. (8)-(10) to two coupled equations, on the effective variables $\Phi = e\phi/T_e = \sum Z_s\tilde{n}_s/n_{e,0}$ and $\tilde{\tilde{u}}_\parallel = \sum Z_s C_s \tilde{u}_{\parallel,s}$, where $C_s = n_{s,0}/n_{e,0}$ is the equilibrium concentration of species s. The two coupled equations write

$$\partial_t \left(1 - \bar{\rho}^2\nabla_\perp^2\right)\Phi \;+\; v_{*,e}\,\partial_y\Phi \;+\; \nabla_\parallel\tilde{\tilde{u}}_\parallel \;=\; 0 \tag{11}$$

$$\partial_t\tilde{\tilde{u}}_\parallel \;-\; \overline{\nabla u_\parallel}\,\rho_{c,i}v_{T,i}\,\partial_y\Phi \;=\; -c_s^2\nabla_\parallel\Phi \tag{12}$$

where

$$\bar{\rho}^2 \;=\; \sum_{s\neq e} C_s Z_s^2 \rho_{c,s}^2 \tag{13}$$

is a linear combination of ion Larmor radii, $v_{*,e} = T_e/(eBL_{n,e})$ is the electron diamagnetic drift velocity, c_s is the ion-acoustic velocity including the contribution of impurities,

$$c_s^2 \;=\; \sum_{s\neq e} C_s\, Z_s^2\, \frac{T_e}{m_s} \tag{14}$$

(recalling we adopt the cold ion limit), and, most importantly,

$$\overline{\nabla u_\parallel} \;=\; \sum_{s\neq e} C_s\, Z_s\, \nabla u_{\parallel,s,0} \tag{15}$$

is a linear combination of main ion and impurity parallel velocity gradients, which we refer to as the *effective flow shear*. It is the source of free-energy of the i-PVG instability. Note that throughout this paper, we note the radial gradient ($\partial/\partial x$) as ∇ (without a subscript). Let us define the ratio of parallel velocity gradients, $V = \nabla u_{\parallel,z,0}/\nabla u_{\parallel,i,0}$. Then the effective flow shear can also be written as $\overline{\nabla u_\parallel} = (C_i + V\,C_Z\,Z_Z)\,\nabla u_{\parallel,i,0}$.

The above model can in fact be seen as a modification of the Hasegawa-Mima model, including the effective flow shear. This analogy is however limited to the linear regime: a similar linear combination on the system Eqs. (5)-(7) would not yield a comparable effective description of the instability at the non-linear level. However, the nonlinear evolution of a i-PVG wave packet interacting with mesoscale fluctuations (such as convective cells, zonal flows, streamers) can be investigated by modulational analysis [KBLO24].

Fourier analysis yields the dispersion relation,

$$\omega^2 \;-\; \omega_{\mathrm{iDW}}\,\omega \;-\; \frac{\left(k_\parallel c_s\right)^2}{1 \;+\; \left(k_\perp\bar{\rho}\right)^2}\left(1 - \frac{k_y}{k_\parallel}\frac{\overline{\nabla u_\parallel}}{\overline{\omega_c}}\right) \;=\; 0 \tag{16}$$

where

$$\omega_{\mathrm{iDW}} \;=\; \frac{k_y\, v_{*,e}}{1 \;+\; \left(k_\perp\bar{\rho}\right)^2} \tag{17}$$

is the drift-wave frequency modified by impurities, and

$$\overline{\omega_c} \;=\; \sum_{s\neq e} C_s\, Z_s\, \omega_{c,s} \tag{18}$$

is a linear combination of main ion and impurity cyclotron frequencies.

The quadratic Eq. (16) includes an unstable solution if and only if the function

$$\Delta(k_\parallel) \;=\; \left(\frac{\omega_{iDW}}{2}\right)^2 + \frac{\left(k_\parallel c_s\right)^2}{1 \,+\, \left(k_\perp \overline{\rho}\right)^2}\left(1 - \frac{k_y}{k_\parallel}\frac{\overline{\nabla u_\parallel}}{\overline{\omega_c}}\right) \tag{19}$$

is negative.

When the parallel wave number is $k_\parallel = k_{\parallel,\max}$, with

$$k_{\parallel,\max} \;=\; \frac{\overline{\nabla u_\parallel}}{2\,\overline{\omega_c}}\,k_y \tag{20}$$

the function Δ reaches its minimum value

$$\Delta_{min} \;=\; \left(\frac{\omega_{iDW}}{2}\right)^2 \left(1 \,-\, L_{n,e}^2\left(1 + k_\perp^2\bar{\rho}^2\right)\frac{\overline{\nabla u_\parallel}^2}{\overline{c_s}^2}\right) \tag{21}$$

Therefore, the linear instability condition can be written in terms of the effective flow shear, $\left|\overline{\nabla u_\parallel}\right| > \overline{\nabla u_\parallel}_{\rm cr}$ with

$$\overline{\nabla u_\parallel}_{\rm cr}^2 \;=\; \frac{\left(c_s/L_{n,e}\right)^2}{1 + \left(k_\perp\overline{\rho}\right)^2} \tag{22}$$

or, alternatively, in terms of the main ion flow shear, $\left|\nabla u_{\parallel,i,0}\right| > \nabla u_{i,\rm cr}$ with

$$\nabla u_{i,\rm cr} \;=\; \frac{1}{C_i + V\,C_Z\,Z_Z}\overline{\nabla u_\parallel}_{\rm cr} \tag{23}$$

When an i-PVG wave is unstable, its frequency is $\omega_{\rm iDW}/2$ and its growth rate is $\gamma = \sqrt{-\Delta}$ (Δ is then negative). These expressions are given in Eqs. (17) and (19). Note that the factor 2 in the frequency is mainly due to the finite value of $k_\parallel$ – the i-PVG frequency does recover the impurity-modified drift-wave frequency in the limit of $k_\parallel = 0$ and $\overline{\nabla u_\parallel} = 0$.

For a given set of plasma parameters and a given value of $k_\perp$, the maximum growth rate is reached for $k_x = 0$ and $k_\parallel = k_{\parallel,\max}(k_y)$, in which case

$$\gamma_{max} \;=\; \frac{k_\perp\, v_{*,e}/2}{1 \,+\, k_\perp^2\bar{\rho}^2}\left[L_{n,e}^2\left(1 + k_\perp^2\bar{\rho}^2\right)\frac{\overline{\nabla u_\parallel}^2}{c_s^2} \,-\, 1\right]^{1/2} \tag{24}$$

Hereafter we focus on that case $k_x = 0$, which is also more consistent with our local model.

4 Application to typical plasmas

For concision, let us note $M = m_z/m_i$ the mass ratio, and $V = \nabla u_{\parallel,z,0}/\nabla u_{\parallel,i,0}$ the ratio of parallel velocity gradients. Table 1 shows the parameters of a reference case, designed to be representative of a fusion plasma with highly ionized tungsten. The values $\nabla u_{\parallel,i,0}$ and $V = 2$ are consistent with measurements [TGF+02, GCH+19]. Hereafter, we present analyses of cases which are variations of this reference case. The varying parameters are summarized in Table 2.

	$L_n/\rho_{c,i}$	$\nabla u_{\parallel,i,0}/\omega_{c,i}$	V	M	Z	C_z	$\rho_{c,i}k_x$	$\rho_{c,i}k_y$	$\rho_{c,i}k_\parallel$
Reference case	10	0.1	2	184	40	10^{-3}	0	0.7	$\rho_{c,i}k_{\parallel,\max}$

Table 1: Input parameters for the reference case.

	$\nabla u_{\parallel,i,0}/\omega_{c,i}$	V	M	Z	C_z	$\rho_{c,i}k_y$	$\rho_{c,i}k_\parallel$
Fig. 1	0.1	2	12 and 184	6 and 40	0 and 10^{-3}	0.7	-0.02 – 0.08
Fig. 2	0.1	2	184	40	10^{-3}	-1 – 1	-0.1 – 0.1
Fig. 3	0.1	2	12 and 184	6 and 40	0 and 10^{-3}	0 – 2	$\rho_{c,i}k_{\parallel,\max}$
Fig. 4	-	2	0 – 200	0 – 200	10^{-3}	0.7	$\rho_{c,i}k_{\parallel,\max}$
Fig. 5	0.1	-1 – 2	5 – 200	5	10^{-4} – 10^{-2}	0.7	$\rho_{c,i}k_{\parallel,\max}$
Fig. 6	0.1	-1 – 2	184	0 – 50	10^{-4} – 10^{-2}	0.7	$\rho_{c,i}k_{\parallel,\max}$
Fig. 7	0.1	-1 – 2	12 – 184	3 – 40	10^{-5} – 10^{-2}	0.7	$\rho_{c,i}k_{\parallel,\max}$
Fig. 8	0.08	2	12 and 184	6 and 40	0 and 10^{-3}	0 – 2	$\rho_{c,i}k_{\parallel,\max}$
Fig. 9	0.08	2	0 – 200	0 – 200	10^{-3}	0.7	$\rho_{c,i}k_{\parallel,\max}$
Fig. 10	0.08	-1 – 2	5 – 200	5	10^{-4} – 10^{-2}	0.7	$\rho_{c,i}k_{\parallel,\max}$
Fig. 11	0.08	-1 – 2	184	0 – 50	10^{-4} – 10^{-2}	0.7	$\rho_{c,i}k_{\parallel,\max}$
Fig. 12	0.08	-1 – 2	12 – 184	3 – 40	10^{-5} – 10^{-2}	0.7	$\rho_{c,i}k_{\parallel,\max}$

Table 2: Input parameters for each figure. This table includes only parameters which vary compared to the reference case. In other words, for all figures, $L_n/\rho_{c,i} = 10$ and $k_x = 0$.

4.1 Dispersion relation

Figure 1 shows the dispersion relation for the reference case, as well as for C^{6+} ($M = 12$ and $Z = 6$) impurity. The dispersion relation of the pure PVG is included for comparison. We observe that the dispersion relation is qualitatively similar for the pure and impure cases, but quantitatively different. As demonstrated hereafter, differences are more important closer to the PVG instability threshold, or for higher impurity concentrations.

Let us now verify both the accuracy of the assumptions (i)–(iv) described in Sec. 3, and the correctness of our linear analysis. We developed an initial value numerical simulation code to solve the fluid model Eqs. (5-7), which does not rely on the assumptions (i)–(iv). Time integration is performed by an explicit RK4 scheme with time-step width $\Delta t = 10^{-2}\omega_{c,i}^{-1}$. All quantities ($\phi$, n_s, $u_{\parallel,s}$) are described in Fourier space (k_x, k_y) on a 256x256 grid for a fixed $k_\parallel$. Nonlinear terms such as $n_s\, u_{\parallel,s}$ are computed in real space before being transformed back to Fourier space. Fig. 1 includes the frequency and growth rate extracted from time-traces of complex Fourier component of ϕ, during the linear phase. There is good quantitative agreement for the values of $k_\parallel$ such that the growth rate is close to its maximum – the relative error for the growth rate remains below 0.2% for the range $\gamma/\omega_{c,i} > 0.014$. The relative error can be as high as a few percent in the range $0.004 < \gamma/\omega_{c,i} < 0.007$ or a few tens of percent in the range $\gamma/\omega_{c,i} < 0.004$, but these weak modes are negligible in the linear phase of the instability. The relative error for the frequency remains below 0.5% for the whole unstable range.

Figure 2 shows the linear growth rate in the space of wavevector components ($k_\parallel$, k_y). The asymmetry in this space, instability occurring only for $k_y\, k_\parallel > 0$ (for $\overline{\nabla u_\parallel} > 0$), is an important property of the i-PVG. If the sign of $\overline{\nabla u_\parallel}$ was flipped, the unstable region would be in the region $k_y\, k_\parallel < 0$. As expected, growth rate is maximum for $k_\parallel = k_{\parallel,\max}$. Hereafter, we always set $k_\parallel = k_{\parallel,\max}$.

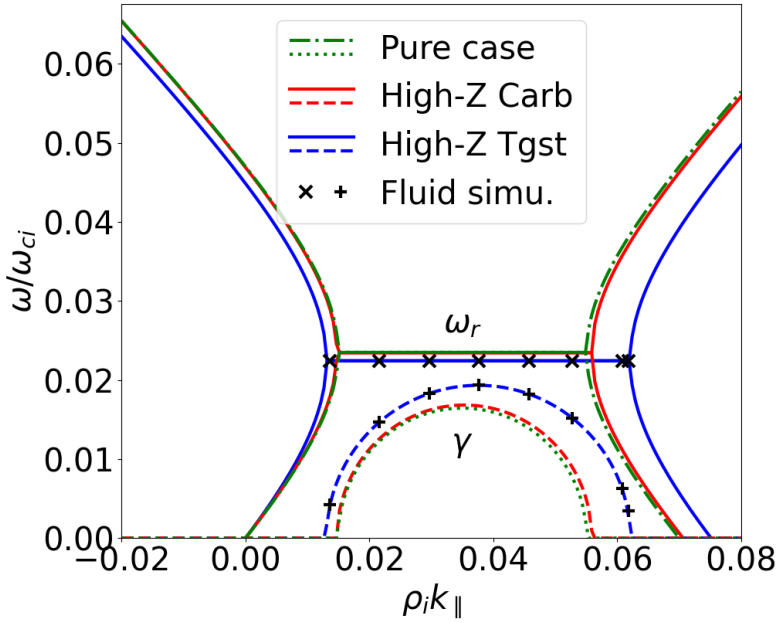

Figure 1: Dispersion relation of the i-PVG: frequency and growth rate against parallel wavenumber, for the reference case ("High-Z Tgst"), as well as a case with C^{6+} impurity ("High-Z Carb"). The dispersion relation of the pure PVG is included for comparison. The curves for the pure PVG are almost hidden behind the curves for the C^{6+} impurity. The cross and plus symbols correspond to linear frequency and growth rate measured in an initial value simulation of the fluid model Eqs. (5-7).

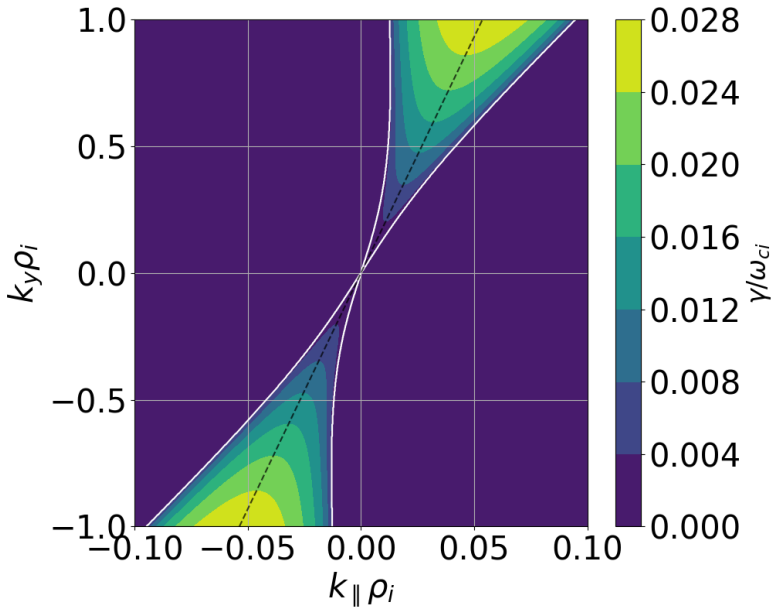

Figure 2: Growth rate against parallel and azimuthal wavenumbers, for the reference case. The dashed black line represents the condition $k_\parallel = k_{\parallel,\max}$. The white curve is the instability threshold.

Figure 3 displays the maximum growth rate (obtained for $k_\parallel = k_{\parallel,\max}$) against the azimuthal k_y wavenumber, as well as the corresponding frequency. Our model does not include any mechanism for small scale dissi-

pation. As a consequence, $\gamma_{\max}$ spuriously keeps on increasing for increasing k_y. However, our model looses its validity as $\rho_{c,i}k$ approaches unity. With the knowledge of the typical shape of $\gamma_{\max}(k)$ obtained from more complete models for many instabilities, let us approximate the physical maximum growth rate by choosing a cut-off at $\rho_{c,i}k = 0.7$ as a first, qualitative approach. Then, for our reference case, the maximum growth rate is $\gamma_{\max} \sim 0.02\,\omega_{ci}$.

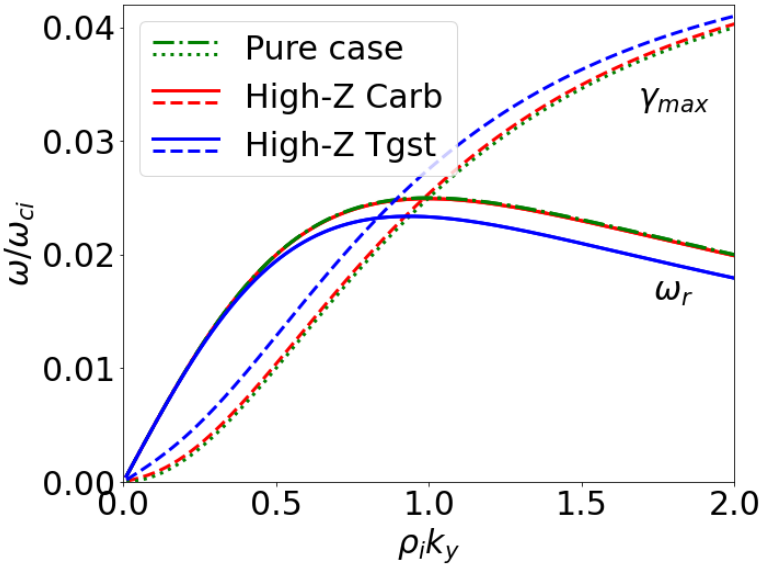

Figure 3: Dispersion relation of the i-PVG: frequency and growth rate against the azimuthal wavenumber k_y, for the reference case ("High-Z Tgst"), as well as a case with C^{6+} impurity ("High-Z Carb"). The dispersion relation of the pure PVG is included for comparison. The curves for the pure PVG are almost hidden behind the curves for the C^{6+} impurity.

In summary, the results in this section confirm that the linear properties of the i-PVG instability are qualitatively the same as that of the pure PVG instability. For the chosen set of parameters, even the quantitative differences are small. However, that is for a case where the pure PVG instability is already quite strong, since $\gamma \approx \omega$. In this sense, the above results concern a range far from instability threshold. By contrast, in the next section we focus on the instability threshold itself.

4.2 Critical ionic PVG

As explained in Sec. 3, for a given set of parameters (L_n, $\nabla u_{\parallel,i,0}$, V, M, Z, C_z), and bounded value of k_y, the i-PVG instability threshold can be expressed either in terms of the effective flow shear, which is a combination of main ion and impurity flow shears, or, alternatively, in terms of the main ion flow shear alone. The corresponding thresholds are given by Eqs. (22) and (23), respectively. The preferred point-of-view may depend on the experimental conditions which determine preferred control parameters. Here we focus on the second point-of-view, that of critical main ion flow shear for a given ratio V.

Figure 4 displays the critical main ion flow shear against mass and charge ratios, for $V = 2$ and $C_z = 10^{-3}$. It is clear that i-PVG-unstable conditions are more readily reached when the impurity is massive and highly ionized. In realistic machines however, radiation from high-mass and high-Z impurities is a severe issue, so that the applicability of such ranges of parameters should be carefully studied. On the contrary, at this low concentration, the threshold for low-mass, low-charge impurities is not so different from the threshold for high-mass, low-charge impurities, and is actually close to the threshold of the pure PVG.

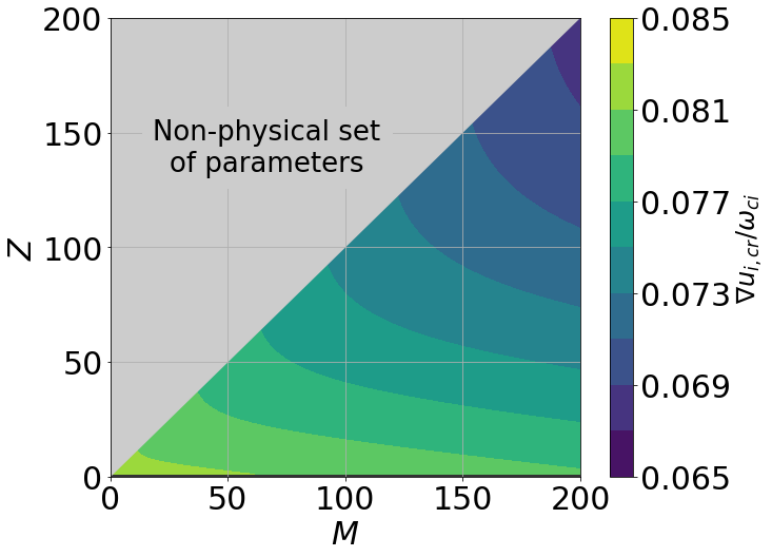

Figure 4: Critical main ion flow shear against mass and charge ratios.

Figure 5 illustrates the role of the mass ratio, at fixed $Z = 5$, for various impurity concentrations C_z and various flow shear ratios V. The critical main ion flow shear is always decreasing with increasing mass ratio, but the relationship is nonlinear. Here the impact of V is small, but that is because C_z and Z are both low, such that the i-PVG is actually very close to the pure PVG.

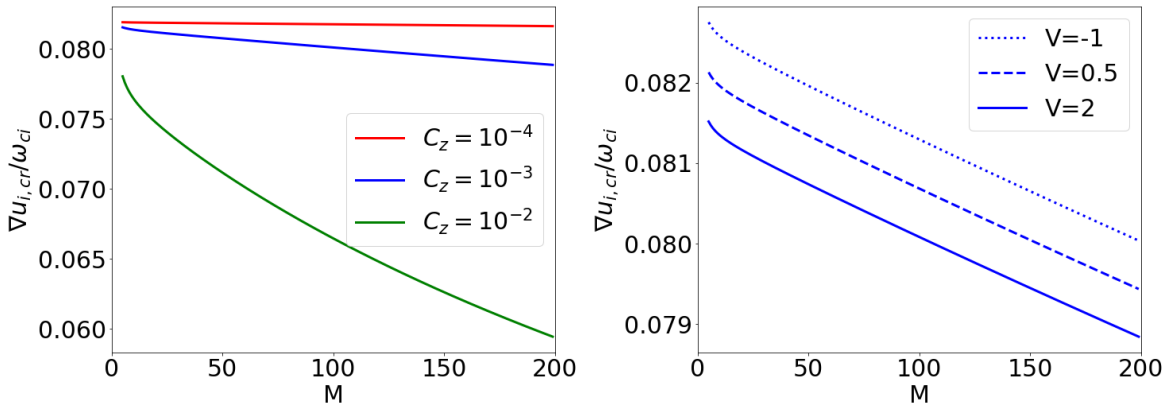

Figure 5: Critical main ion flow shear against mass ratio, for $Z = 5$. Left: fixed $V = 2$ and various concentrations. Right: fixed $C_z = 10^{-3}$ and various V.

Figure 6 illustrates the role of the charge number Z of the impurity, at fixed mass ratio $M = 184$ (tungsten), for various impurity concentrations C_z and various flow shear ratios V. Higher Z can be either stabilising or destabilising depending on the parameters, such as V. Here, at concentration $C_z = 10^{-3}$, it is stabilising for $V = 2$, but destabilising for $V = 0.5$ and $V = -1$. This stabilising role of impurities is consistent with simple intuition in the case $V = -1$, since impurity flow counteracts main ion flow in this case. In the case $V = 0.5$, the stabilising effect is more subtle: in this case the variation in Eq. (23) is dominated by the denominator $(C_i + VC_Z Z)$, which can be re-written as $[1 + ZC_Z(V - 1)]$. However, which term dominates

depends on the value of V. For example, for $V = 1$, the variation as Z increases is dominated by the decrease of c_s, so increasing Z is stabilising. For an intermediate case, $V = 0.8$, the dependency is non-monotonous: increasing Z is stabilising for $Z < 28$ and destabilising for $Z \geq 28$.

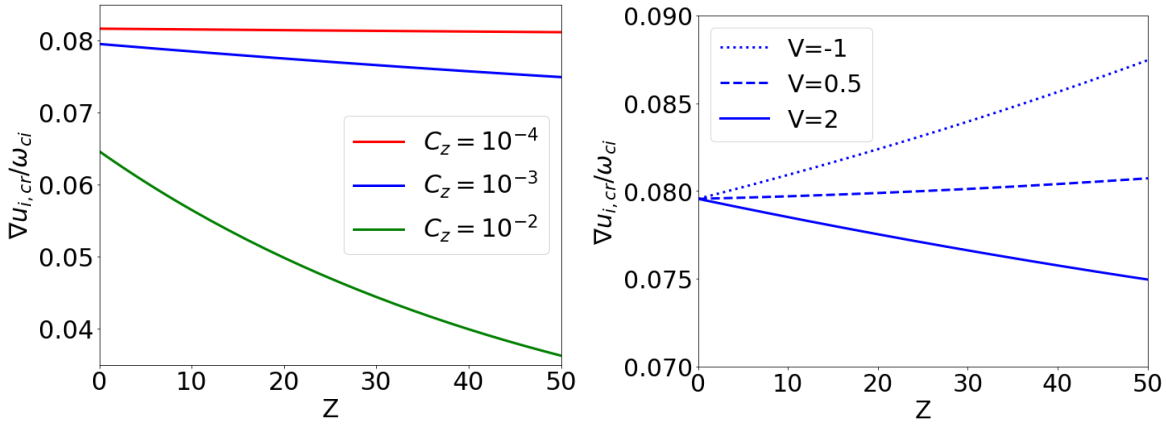

Figure 6: Critical main ion flow shear against charge number Z, for $M = 184$. Left: fixed $V = 2$ and various concentrations. Right: fixed $C_z = 10^{-3}$ and various V.

A more intuitive picture can be obtained by varying impurity concentration while the impurity species and Z are fixed. Figure 7 illustrates the role of impurity concentration, for various impurity species (C^{3+}, C^{6+}, W^{5+}, W^{40+}) and various values of V. From this point of view, the role of impurity flow is consistent with simple intuition: if $V > 0$, impurity flow adds up to main ion flow, which is destabilising; conversely, if $V < 0$, impurity flow counters main ion flow, which is stabilising. Increasing concentration accentuates the impact – whether stabilising or destabilising – of the impurity on the instability threshold. This effect may offer new means of control of the PVG instability by impurity injection.

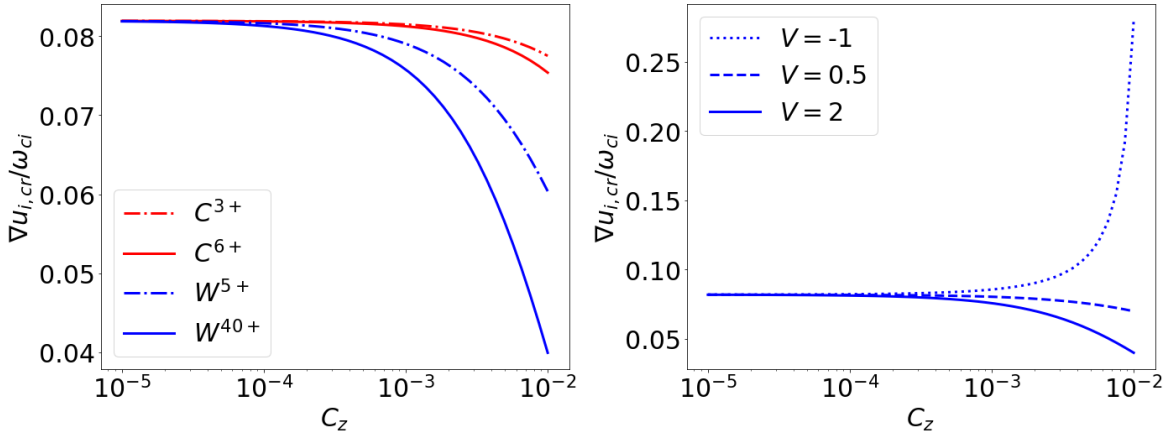

Figure 7: Critical main ion flow shear against impurity concentration. Left: fixed $V = 2$ and various species. Right: various V and the impurity is W^{40+}.

In summary, the critical main ion flow shear decreases non-linearly with increasing mass ratio, and may increase or decrease in a non-trivial manner depending on all the other parameters.

For our reference case, the instability threshold is $\nabla u_{i,\mathrm{cr}} = 0.075925\,\omega_{c,i}$. In the next subsection, in order to study the growth rate near the instability threshold, we arbitrarily fix $\nabla u_{\parallel,i,0} = 0.08\,\omega_{c,i}$.

4.3 Growth rate

Figure 8 displays the maximum growth rate (obtained for $k_\parallel = k_{\parallel,\max}$) against the azimuthal k_y wavenumber, as well as the corresponding frequency, for $\nabla u_{\parallel,i,0} = 0.08\,\omega_{c,i}$. Here, for $k_y < 0.75\,\rho_{c,i}^{-1}$, the main ion parallel velocity shear is below the threshold for pure PVG. As a consequence, the behavior is qualitatively different compared to Fig. 1 (which is for $\nabla u_{\parallel,i,0} = 0.1\,\omega_{c,i}$, above the pure PVG threshold even for $k_y \to 0$). There is now an additional bifurcation.

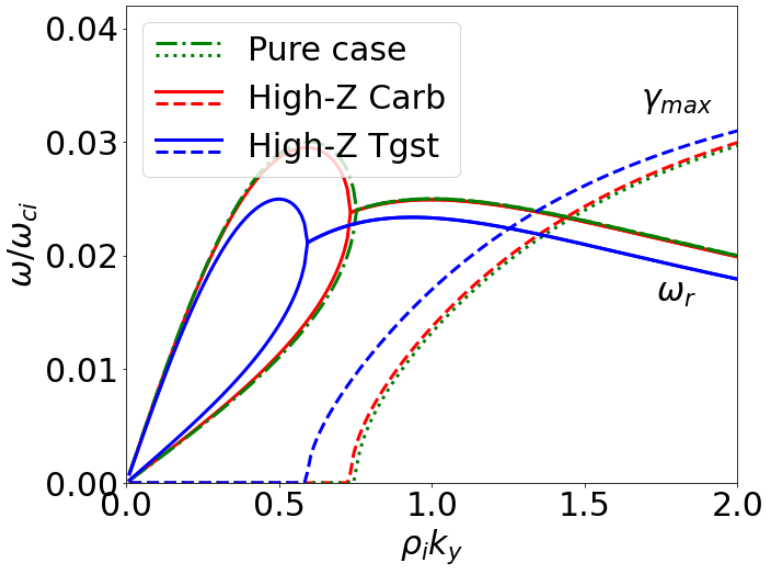

Figure 8: Dispersion relation of the i-PVG: frequency and growth rate against azimuthal wavenumber, for the reference case, as well as a case with C^{6+} impurity ("High-Z Carb") – same as Fig. 1 but for lower $\nabla u_{\parallel,i,0} = 0.08\,\omega_{c,i}$. The dispersion relation of the pure PVG is included for comparison. The curves for the pure PVG are almost hidden behind the curves for the C^{6+} impurity.

Again, let us approximate the physical maximum growth rate by fixing $\rho_{c,i}k = 0.7$. Then, for our plasma with W^{40+}, the maximum growth rate is $\gamma_{\max} \sim 0.008\,\omega_{c,i}$. Consistently, the maximum growth rate in the following figures (9, 10, 11 and 12), where impurity parameters are varied, is obtained from our model for the wave vector $\boldsymbol{k}_{\max}$ with components $k_x = 0$, $k_y = 0.7/\rho_{c,i}$, $k_\parallel = k_{\parallel,\max}$.

Figure 9 shows our estimated maximum growth rate against mass and charge ratios, for $V = 2$ and $C_z = 10^{-3}$. Recalling that the real frequency of the mode is typically $\omega \approx 0.02\,\omega_{c,i}$, we confirm that our choice of cut-off ($\rho_{c,i}k = 0.7$) ensures that $\gamma_{\max}/\omega$ remains significantly below unity, except for unrealistically highly ionized heavy impurities. Note that here, the main ion parallel velocity shear is below the threshold for pure PVG (which is $0.08192\,\omega_{c,i}$ for $k_y = 0.7\,\rho_{c,i}^{-1}$).

Figure 10 illustrates the role of the mass ratio on the maximum growth rate, for fixed $Z = 5$ and various C_z and V. From this perspective, the instability threshold can be viewed as a threshold in impurity mass, every other parameters being fixed. Similarly to the effect of mass on the instability threshold, increasing mass always increases the maximum growth rate.

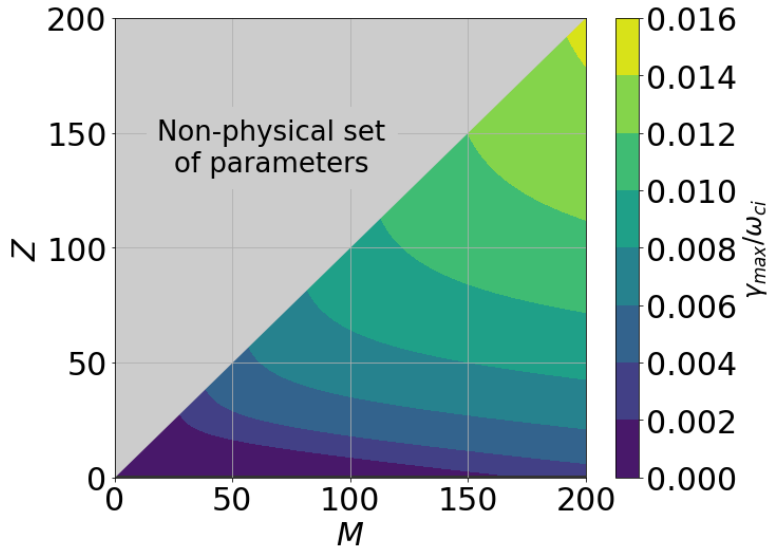

Figure 9: Maximum growth rate against mass and charge ratios, for $\nabla u_{\parallel,i,0} = 0.08\,\omega_{c,i}$.

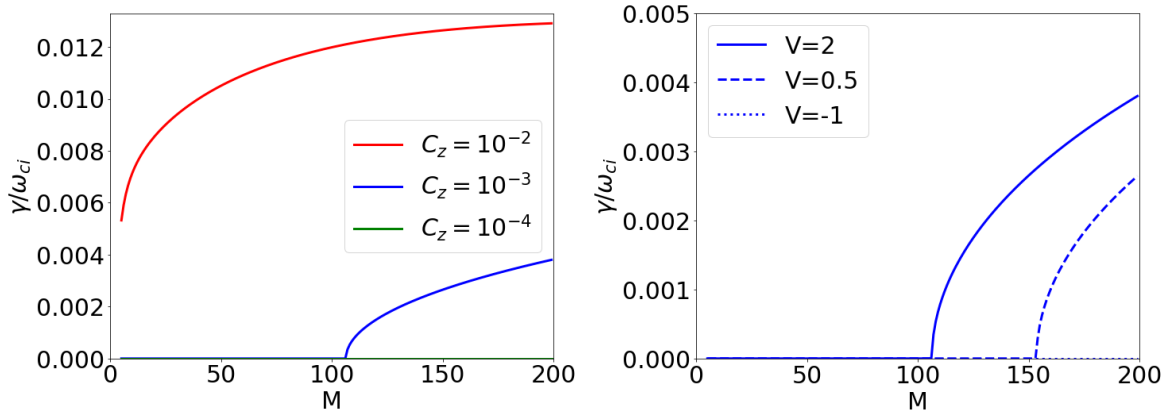

Figure 10: Maximum growth rate against mass ratio, for $\nabla u_{\parallel,i,0} = 0.08\,\omega_{c,i}$ and $Z = 5$. Left: fixed $V = 2$ and various C_z. Right: fixed $C_z = 10^{-3}$ and various V.

Figure 11 illustrates the role of the impurity charge on the maximum growth rate, for fixed $M = 184$ and various C_z and V. As a rule of thumb, the growth rate is less sensitive to Z than to M. Increasing Z may be destabilising or stabilising depending on the parameters, and in particular depending on the flow shear ratio V. For $V = 0.5$ or $V = -1$, the i-PVG instability threshold can be viewed as a threshold in impurity charge, instability occurring only *below* a critical number.

Figure 12 illustrates the role of impurity concentration on the maximum growth rate, for various species and V. In this point-of-view, the instability threshold is a threshold in concentration. With our arbitrary choice of $\nabla u_{\parallel,i,0} = 0.08\,\omega_{c,i} = 1.05\nabla u_{i,\mathrm{cr}}$, the concentration threshold is of the order of 10^{-4} – 10^{-3} for tungsten, and of the order of 10^{-3} – 10^{-2} for carbon. However, with $\nabla u_{\parallel,i,0}$ closer to $\nabla u_{i,\mathrm{cr}}$, the concentration threshold can even be much lower. Here, the growth rate increases with increasing concentration. However, there are also cases where concentration has a non-monotonous impact [LBK23].

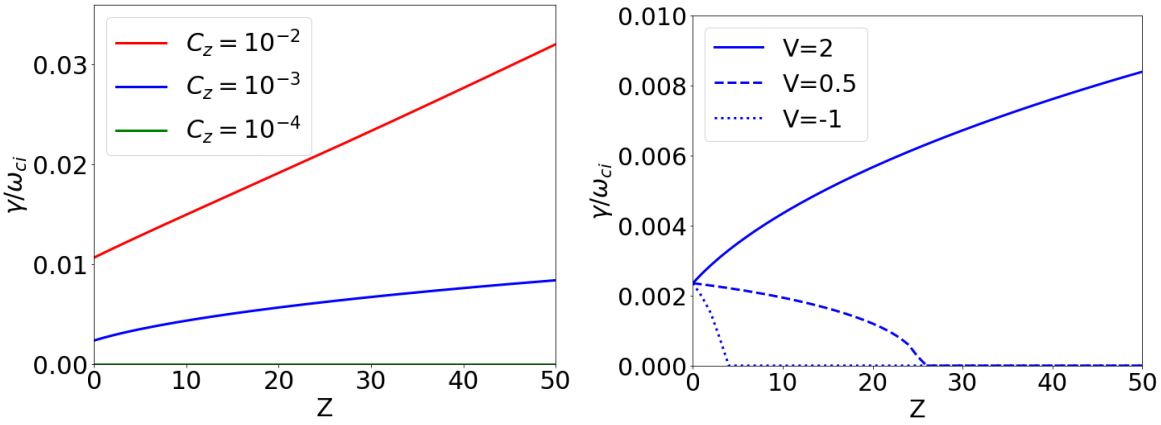

Figure 11: Maximum growth rate against impurity charge, for $\nabla u_{\parallel,i,0} = 0.08\,\omega_{c,i}$ and $M = 184$. Left: fixed $V = 2$ and various concentrations. Right: fixed $C_z = 10^{-3}$ and various V.

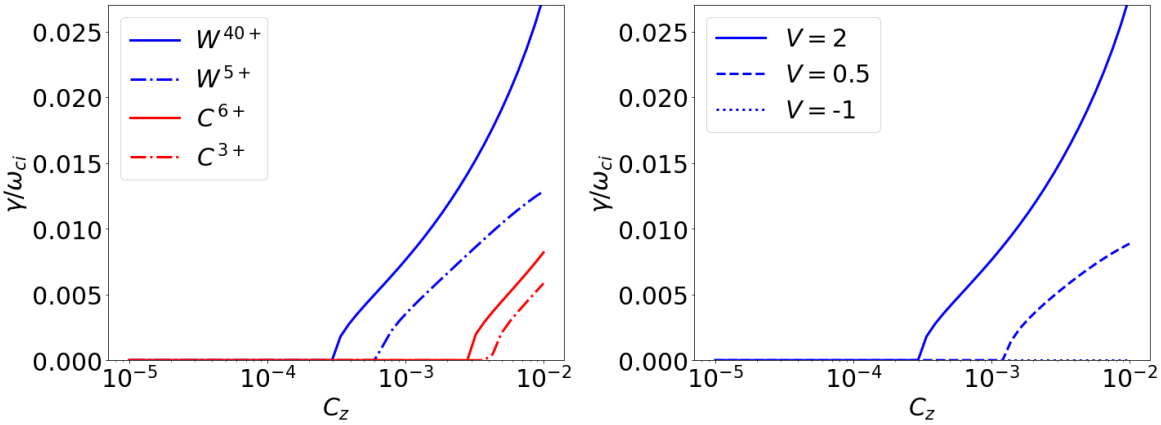

Figure 12: Maximum growth rate against impurity concentration. Left: fixed $V = 2$ and various species. Right: various V and the impurity is W^{40+}.

Let us emphasize that figures 11 and 12 are useful to guide experiments which could test this theory. For example, impurities may be purposely injected in a linear device, to either excite the i-PVG, or to suppress a pure PVG (depending on the direction of flow shears). However, the analysis should be reproduced after measuring the values of parallel flows, since the thresholds in Z and C_Z are sensitive to the value of the main ion flow shear – and more specifically its closeness to marginal stability.

5 Conclusions and discussions

We investigated the role of a radial gradient of the parallel flow of impurities in a magnetized plasma. The linear dispersion relation indicates that the impurity-PVG is destabilised when $L_{n,e}^2 \overline{\nabla u_\parallel}^2 > c_s^2/[1 + (k_\perp \overline{\rho})^2]$. Similarly to the pure-PVG, the i-PVG is asymmetric in the space of wavevector components ($k_\parallel$, k_y): it is unstable only for $k_y\, k_\parallel \overline{\nabla u_\parallel} > 0$.

If the plasma is unstable to the pure-PVG, then impurities can be stabilising if their flow shear is opposite to the flow shear of main ions. Note that this does not require flows themselves to be in opposite directions. The

role of impurities is more prominent for higher mass and/or higher charge number. In general, the instability threshold and the growth rate are more sensitive to charge number than to mass.

The analytic expression of the maximum growth rate is given in Eq. (24). To investigate how the maximum growth rate depends on plasma and impurity parameters (Figs. 10-12), we assumed a perpendicular wavenumber comparable to the inverse Larmor radius (of main ions).

In the typical case of a hydrogen plasma with a 10^{-3} concentration of W^{40+}, tungsten flow shear being twice the hydrogen flow shear, and assuming that the linear growth rate is maximum for $k_\perp \approx 0.7\,\rho_{c,i}^{-1}$, the i-PVG instability is unstable for hydrogen flow shear above a threshold $\nabla u_{i,\mathrm{cr}} \approx 0.076\,\omega_{c,i}$, and most unstable for parallel wavenumbers $k_\parallel \approx 0.04\,\rho_{c,i}^{-1}$.

Although the present work should in principle capture the main linear properties of the i-PVG, the reader should keep in mind that it is subject to several caveats: it is a local analysis, assuming cold ions and Boltzmann electrons. Our model does not include collisional effects, viscosity, resistivity. We limited our analysis to two species, but it can be straightforwardly generalised to more species.

The present work focused on the linear properties of the i-PVG. Although, the (quasi-)steady-state spectrum of fluctuations may roughly reflect the location in $\boldsymbol{k}$-space of most unstable modes, nonlinear simulations and analysis are necessary to improve predictions and understanding of steady-state fluctuations. In particular, the present work cannot address the role of zonal flows, which can be generated by PVGs [KII17]. Impurities may play an interesting role in both the generation and the damping of zonal flows.

Impurities are transported in the radial direction, in general by both neoclassical and turbulent processes, although one process may dominate depending on the species and plasma parameters. The efficiency of fusion depends on the radial distribution of impurities, which results from transport. For example, slight tungsten contamination of the core yields prohibitive energy losses. Therefore, it is essential to improve our understanding of impurity transport. However, the model adopted here assumes a Boltzmann response of electrons to electric fluctuations, which precludes any radial transport of electrons. Quasi-neutrality then forces impurity particle transport to exactly balance main ion particle transport. This assumption is reasonable for the present linear analysis, but is too strong for providing any conclusion about impurity particle transport. The relaxation of this assumption is left for future work. In addition, we recall that our model assumes cold ions, which precludes us from making any similar statement about heat transport.

Acknowledgments

This work was supported by a scholarship by Kyushu University, the joint research project in RIAM, the Grants-in-Aide for Scientific Research of JSPS of Japan (JP21H01066, JP23K20838), a grant from the Chaire Energies Durables of Ecole Polytechnique, and funding from the Agence Nationale de la Recherche for the project GRANUL (ANR-19-CE30-0005).

References

[BPH+11] M. Barnes, F. Parra, E. Highcock, A. Schekochihin, S. Cowley, and C. Roach, Turbulent transport in tokamak plasmas with rotational shear, *Phys. Rev. Lett.* **106** no. 17 (2011), 175004. doi:10.1103/PhysRevLett.106.175004.

[BGH+23] F. Brochard, D. Geneve, S. Heuraux, V. Bobkov, D. Del Sarto, E. Faudot, A. Ghizzo, E. Gravier, N. Lemoine, M. Lesur, N. Louis, J. Moritz, T. Reveillé, V. Rohde, U. Stroth, G. Urbanczyk, F. Volpe, and H. Zohm, Spektre, a linear radiofrequency device for investigating

edge plasma physics, in *49th EPS Conference on Plasma Physics*, IAEA Publications, Vienna, 2023, p. THS/P5–03.

[CRL73] P. J. Catto, M. N. Rosenbluth, and C. Liu, Parallel velocity shear instabilities in an inhomogeneous plasma with a sheared magnetic field, *Phys. Fluids* **16** no. 10 (1973), 1719–1729. doi:10.1063/1.1694200.

[CBKW12] I. Chapman, S. Brown, R. Kemp, and N. Walkden, Toroidal velocity shear kelvin–helmholtz instabilities in strongly rotating tokamak plasmas, *Nucl. Fusion* **52** no. 4 (2012), 042005. doi:10.1088/0029-5515/52/4/042005.

[DG66] N. D'angelo and S. V. Goeler, Investigation of the kelvin-helmholtz instability in a cesium plasma, *Phys. Fluids* **9** no. 2 (1966), 309–313. doi:10.1063/1.1761674.

[D'A65] N. D'Angelo, Kelvin—helmholtz instability in a fully ionized plasma in a magnetic field, *Phys. Fluids* **8** no. 9 (1965), 1748–1750. doi:10.1063/1.1761496.

[DHG+92] J. Drake, A. Hassam, P. Guzdar, C. Liu, and D. McCarthy, Loss of static equilibrium, flow generation and the development of turbulence at the edge of tokamaks, *Nucl. Fusion* **32** no. 9 (1992), 1657. doi:10.1088/0029-5515/32/9/I15.

[FDG+12] A. Field, D. Dunai, R. Gaffka, Y.-c. Ghim, I. Kiss, B. Meszaros, T. Krizsanoczi, S. Shibaev, and S. Zoletnik, Beam emission spectroscopy turbulence imaging system for the mast spherical tokamak, *Rev. Sci. Instr.* **83** no. 1 (2012), 013508. doi:10.1063/1.3669756.

[GSG+02] X. Garbet, Y. Sarazin, P. Ghendrih, S. Benkadda, P. Beyer, C. Figarella, and I. Voitsekhovitch, Turbulence simulations of transport barriers with toroidal velocity, *Phys. Plasmas* **9** no. 9 (2002), 3893–3905. doi:10.1063/1.1499494.

[GCH+19] B. Grierson, C. Chrystal, S. Haskey, W. Wang, T. Rhodes, G. McKee, K. Barada, X. Yuan, M. Nave, A. Ashourvan, and C. Holland, Main-ion intrinsic toroidal rotation across the itg/tem boundary in diii-d discharges during ohmic and electron cyclotron heating, *Phys. Plasmas* **26** no. 4 (2019), 042304. doi:10.1063/1.5090505.

[GWZ19] W. Guo, L. Wang, and G. Zhuang, Impurity transport driven by parallel velocity shear turbulence in hydrogen isotope plasmas, *Nucl. Fusion* **59** no. 7 (2019), 076012. doi:10.1088/1741-4326/ab1967.

[HSC+12] E. Highcock, A. Schekochihin, S. Cowley, M. Barnes, F. Parra, C. Roach, and W. Dorland, Zero-turbulence manifold in a toroidal plasma, *Phys. Rev. Lett.* **109** no. 26 (2012), 265001. doi:10.1103/PhysRevLett.109.265001.

[IKK+16] S. Inagaki, T. Kobayashi, Y. Kosuga, S.-I. Itoh, T. Mitsuzono, Y. Nagashima, H. Arakawa, T. Yamada, Y. Miwa, N. Kasuya, and others, A concept of cross-ferroic plasma turbulence, *Sci. Rep.* **6** no. 1 (2016), 22189. doi:10.1038/srep22189.

[KTH03] T. Kaneko, H. Tsunoyama, and R. Hatakeyama, Drift-wave instability excited by field-aligned ion flow velocity shear in the absence of electron current, *Phys. Rev. Lett.* **90** no. 12 (2003), 125001. doi:10.1103/PhysRevLett.90.125001.

[KIK+16] T. Kobayashi, S. Inagaki, Y. Kosuga, M. Sasaki, Y. Nagashima, T. Yamada, H. Arakawa, N. Kasuya, A. Fujisawa, S.-I. Itoh, and others, Structure formation in parallel ion flow and density profiles by cross-ferroic turbulent transport in linear magnetized plasma, *Phys. Plasmas* **23** no. 10 (2016), 102311. doi:10.1063/1.4965915.

[KBLO24] Y. Kosuga, J. Bourgeois, M. Lesur, and I. Oyama, Breathing impure plasmas, *Plasma Phys. Control. Fusion* **66** no. 7 (2024), 075018. doi:10.1088/1361-6587/ad5105.

[KII17] Y. Kosuga, S.-I. Itoh, and K. Itoh, Zonal flow generation in parallel flow shear driven turbulence, *Phys. Plasmas* **24** no. 3 (2017), 032304. doi:10.1063/1.4978485.

[KII15] Y. Kosuga, S.-I. Itoh, and K. Itoh, Density peaking by parallel flow shear driven instability, *Plasma Fusion Research* **10** (2015), 3401024–3401024. doi:10.1585/pfr.10.3401024.

[LBK23] M. Lesur, J. Bourgeois, and Y. Kosuga, Impurity parallel velocity gradient instability, in *Fusion Energy 2023 (Proc. 29th Int. Conf. London)*, Vienna: IAEA, International Centre, 2023.

[McC02] D. McCarthy, Edge harmonic oscillations produced by toroidal velocity shear, *Phys. Plasmas* **9** no. 6 (2002), 2451–2454. doi:10.1063/1.1472503.

[NCL10] S. L. Newton, S. C. Cowley, and N. F. Loureiro, Understanding the effect of sheared flow on microinstabilities, *Plasma Phys. Control. Fusion* **52** no. 12 (2010), 125001. doi:10.1088/0741-3335/52/12/125001.

[SHC12] A. Schekochihin, E. Highcock, and S. Cowley, Subcritical fluctuations and suppression of turbulence in differentially rotating gyrokinetic plasmas, *Plasma Phys. Control. Fusion* **54** no. 5 (2012), 055011. doi:10.1088/0741-3335/54/5/055011.

[TGF+02] D. Testa, C. Giroud, A. Fasoli, K.-D. Zastrow, and E.-J. Team, On the measurement of toroidal rotation for the impurity and the main ion species on the joint european torus, *Phys. Plasmas* **9** no. 1 (2002), 243–250. doi:10.1063/1.1427727.

[WWY+98] G. Wang, L. Wang, X. Yang, C. Feng, D. Jiang, and X. Qi, Evidence for parallel flow shear instability in the edge plasma of the ct-6b tokamak, *Plasma Phys. Control. Fusion* **40** no. 3 (1998), 429. doi:10.1088/0741-3335/40/3/007.

[WER+15] W. Wang, S. Ethier, Y. Ren, S. Kaye, J. Chen, E. Startsev, and Z. Lu, Distinct turbulence sources and confinement features in the spherical tokamak plasma regime, *Nucl. Fusion* **55** no. 12 (2015), 122001. doi:10.1088/0029-5515/55/12/122001.

Open Plasma Science

Vol. 1, No. 2 (2025)

Regular article

FEQIS: A free–boundary equilibrium solver for integrated modeling of tokamak plasmas

Emiliano Fable*[,1], Giovanni Tardini[1], Louis Giannone[1], and the ASDEX Upgrade Team[a]

[1]Max-Planck-Institut für Plasmaphysik, Boltzmannstr. 2, 85748 Garching, Germany
[a]see the Author list of H. Zohm *et al.*, 2024 *Nucl. Fusion* 64 112001, doi: 10.1088/1741-4326/ad249d

History
Received October 30, 2024
Revised December 19, 2024
Accepted January 27, 2025
Published February 19, 2025

Identifiers
DOI 10.46298/ops.14641
HAL -
ArXiv 2410.13630

Supplementary Material
-

Abstract

A new axisymmetric equilibrium solver has been written, called FEQIS (Flexible EQuIlibrium Solver), which purpose is to be used inside integrated modeling of tokamak plasmas. The FEQIS code solves the Grad–Shafranov equation and the "circuit" equations for the external coils and passive conducting structures that are toroidally connected. The code has been specifically equipped with flexibility in choice of circuit connections, and a stripped–down numerical scheme for the solution of the Grad–Shafranov equation through a structure of multi–level simplifications which can be tested against the required accuracy.

Keywords— tokamak, equilibrium, free-boundary

* Corresponding author: emiliano.fable@ipp.mpg.de

Cite as: Fable *et al.*, FEQIS: A free–boundary equilibrium solver for integrated modeling of tokamak plasmas, *Open Plasma Science* 1, 2 (2025), doi: 10.46298/ops.14641

Contents

1 Introduction

Application of integrated modeling to tokamak full–discharge prediction has in recent times become possible due to the combination of comprehensive transport modeling tools, which describe the dynamics of the thermonuclear plasma, and the integration of said tools into a virtual representation of the actual machine diagnostics, actuation, and control systems. An example of such nested integration is the flight simulator Fenix [JFET21, WDF+24, FJT+22, MFA+23], which is being developed at ASDEX Upgrade (AUG). In this framework, both the plasma dynamics and the feedback from the control system in response to the diagnosed evolution are modeled in a virtual environment.

From the point of view of simulating the plasma dynamics, one of the basic aspects is the calculation of its magnetostatic equilibrium via the Grad–Shafranov equation (GSE) [Sha60], and its evolution on the time scale of induction/resistance with mutual coupling between the plasma and the external conducting coils and structures [BLF84]. The GSE is fundamentally a non–linear equation, requiring a dedicated iteration scheme to converge to a self–consistent solution. However, when run inside an integrated modeling framework that is supposed to be fast enough to be run inter–discharge (or even real–time), it would be desirable to find a way to minimize the computational time spent on this problem, especially if massive numerical parallelization is not readily available.

It is noted here that there is an extensive literature on the problem of solving the GSE, both in fixed or in free–boundary mode [ELSV24, PCF+13, PKF16, RCRF16, HS14, GL04], and sophisticated numerical tools exist that address this problem, such as [Jeo15, HBB+15, HSB+24, AAM15]. More recently, there have been very

interesting attempts to dramatically speed up the computation by replacing the equation solver with a neural network, e.g. exploiting machine learning and artificial intelligence [JKG+24, MAA+24, WSRS24, DFB+22]. This new line of development has the potential of making GSE solvers extremely fast and still accurate.

In this work we have developed a new equilibrium solver specifically devoted to the problem of being computationally simple and fast with flexibility in retaining or not the more time–consuming aspects such as the non-linear iterations. This new code is presently coupled to the ASTRA transport solver [PY91, FAC+13]. In this work this new code, called FEQIS (Flexible EQuIlibrium Solver), is presented in details, and its application inside the flight simulator Fenix is shown and benchmarked against another established equilibrium solver.

In Section 2, the new code FEQIS is described in terms of modes of operation and details of some of the novel algorithms. In Section 3, application inside the flight simulator Fenix is shown, comparing it with another equilibrium solver. In Section 4, conclusions are drawn.

2 Description of FEQIS

FEQIS comprises 5 main modes of operation, plus the possibility to choose between different options in each mode, which will be described in this and in later sections. The 5 main modes of operation are:
1 - Prescribed boundary mode,
2 - Static forward free boundary solution at initialization,
3 - Inverse solution,
4 - Currents dynamics in vacuum,
5 - Full dynamics with plasma.

Moreover, since the code has been specifically written to be used inside fast integrated modeling, focus will be put on the methods to substantially speed it up. At the source, the code is written in Fortran 90 in a modular way, such that it is easy to manage the different algorithms and add new ones. Presently, FEQIS solves the standard GSE, without rotation and without pressure anisotropy. These features will all be added in the future. The possibility of adding ferromagnetic elements is included, however has not been tested yet. The method used for implementing this aspect is that of equivalent magnetization currents.

Note that the mode 3 (inverse solution) means that a minimization problem is solved to find the set of coil currents that best gives a certain plasma shape. No reconstruction mode is implemented, as done for example in other codes used for real–time equilibrium reconstruction during the experiment itself.

2.1 Prescribed boundary mode

First of all, FEQIS can be used as a prescribed boundary Grad–Shafranov solver (PBGSE solver). This means that the plasma boundary, or last–closed–flux–surface (LCFS) is given by the user as a set of (R, Z) points, forming a closed contour, and then FEQIS solves the GSE inside this given boundary, using as inputs the pressure and current profile densities from the core plasma, plus the total plasma current I_p as a constraint value to rescale the plasma current density j_ϕ at each iteration.

The solver uses an annular grid in non–orthogonal carthesian (r, θ) coordinates, with r the local minor radius and θ the carthesian angle. The equation $\Delta^* \psi = \mu_0 R j_\phi$ is thus solved using a standard LAPACK matrix solver. The magnetic axis is adaptively searched for using a least square fit method, such that at convergence, it coincides with the center of the annular grid. Moreover, the radial coordinate grid points at each θ are moved to coincide with the flux surfaces, thus allowing for easier computation of flux–surface–averaged quantities.

In figure (1) an example of the solution equilibrium for a diverted plasma (AUG #34954 at $t = 2.2$ s) is shown. The comparison shows that FEQIS agrees perfectly with SPIDER [I+05, IKMP09] with respect to the

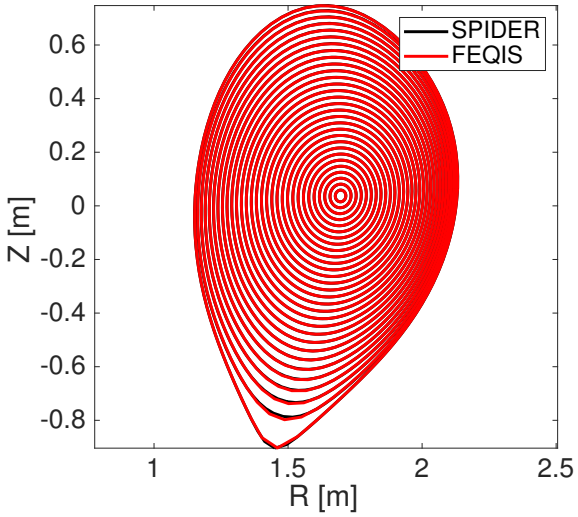

Figure 1: Flux surfaces solved by the PBGSE solver, where the diverted plasma boundary is given as input. Black: SPIDER solution, Red: FEQIS solution.

distribution of flux surfaces (every closed black/red line represents the same equispaced normalized toroidal flux value).

After convergence, several flux–surface–averaged quantities are computed, that are then sent to an output equilibrium structure and can be used in a 1D transport solver like ASTRA.

2.2 Free boundary modes

FEQIS also solves the free–boundary Grad–Shafranov equation (FBGSE), meaning that the magnetic flux boundary conditions are at spatial infinity. For this problem, the Green's function method is promptly employed, to reduce the problem on a closed boundary inside the region of interest [Lac76]. As such, the flux exerted by the coils in the plasma region is computed analytically, and the rectangular grid does not need to encompass all the conducting structures, but can be minimally set around the plasma region (usually just outside the limiter region).

Specifically, the solution grid is Carthesian–rectangular in (R, Z) coordinates, with R being the major radius and Z the vertical axis, in the sense of toroidal cylindrical coordinates, where the toroidal angle φ is ignorable, since we focus on axisymmetric systems.

The FBGSE is solved for using the plasma profiles of pressure and current density, and the external conductor currents. This solution is always "static", as the GSE *per se* has no time derivative term, however the equilibration (or convergence) is obtained in different ways depending on the type of problem solved, which is detailed below. In addition, also in the free boundary problem, the total toroidal plasma current I_p is used as a constraint to rescale the plasma current density at every iteration. The reason for this choice, and where then the total plasma current is computed, will be explained in more details in subsection (2.3.4).

In the following subsections, we analyze the individual modes of operation that are under the category of "free boundary problems". Note that all these modes are not independent in terms of solver usage. In fact they share the same kernel of solvers, that is the solver for the poloidal flux map is the same, as well as the boundary finding routine and the way the equilibrium profiles are mapped on the 2D flux is the same. The only difference between the various modes shown later is in how the coil currents are treated (static, forward, or inverse computation).

2.2.1 Static forward solution at initialization

In this case, the external conductor currents are fixed at their input values (provided by the user), and the solver tries to find a solution using a double iteration strategy.

First, given a guess value of the magnetic axis $(R^0_{\rm mag}, Z^0_{\rm mag})$, the code finds a vertical and radial stabilization field that sets the plasma in that position, adding on top of the real external field provided by the conductors and the plasma itself. This step is performed by starting from the generic flux expression:

$$\psi(R,Z) = \psi_{\rm pl}(R,Z) + \psi_{\rm ext}(R,Z) + \tilde{\psi}_{\rm R} R^2 + \tilde{\psi}_{\rm Z} Z \tag{1}$$

where $\psi_{\rm pl}$ is the poloidal magnetic flux created by the plasma current density, $\psi_{\rm ext}$ the one created by the external conductors, and R, Z the cylindrical coordinates. $\tilde{\psi}_{\rm R}, \tilde{\psi}_{\rm Z}$ are the two stabilizing field constants, and the stabilizing field overall is $\psi_{\rm stab} = \tilde{\psi}_{\rm R} R^2 + \tilde{\psi}_{\rm Z} Z$.

To find the values of the two stabilizing constants, given $AX = (R^0_{\rm mag}, Z^0_{\rm mag})$, we have to solve for the following pair of implicit conditions:

$$\begin{aligned} \left|\frac{\partial \psi}{\partial R}\right|_{AX} &= 0. \\ \left|\frac{\partial \psi}{\partial Z}\right|_{AX} &= 0. \end{aligned} \tag{2}$$

Let us call $\psi_{\rm pl} + \psi_{\rm ext} = \psi_0$. We can thus expand and invert the system (2) to obtain the solution formulas:

$$\begin{aligned} \tilde{\psi}_{\rm R} &= -\frac{1}{2R^0_{\rm mag}} \left|\frac{\partial \psi_0}{\partial R}\right|_{AX} \\ \tilde{\psi}_{\rm Z} &= -\left|\frac{\partial \psi_0}{\partial Z}\right|_{AX} \end{aligned} \tag{3}$$

Obviously, if the plasma have the magnetic axis already coincident with AX, the stabilizing fields will turn out to be 0. To compute the gradients in equation (3) accurately, we expand ψ_0 locally around AX employing a 9–points biquadratic interpolant, i.e. $\psi_0 \approx c_1 R^2 Z^2 + c_2 R^2 Z + c_3 R Z^2 + c_4 R Z + c_5 R^2 + c_6 Z^2 + c_7 R + c_8 Z + c_9$, and use the obtained fit coefficients to compute the gradients analytically. Note that this process is iterated until the current density map $j_\phi(R,Z)$ is converged (as it depends on the actual flux map including the artificial field).

Secondly, an external Newton iteration scheme tries to send to zero the strength of the stabilizing field $(\tilde{\psi}_{\rm R}, \tilde{\psi}_{\rm Z}) \to 0$, by moving around the reference magnetic axis values:

$$\delta(R,Z)_{AX} = -\mathbf{C} \times (\tilde{\psi}_{\rm R}, \tilde{\psi}_{\rm Z}) \tag{4}$$

with $\mathbf{C}$ the 2 X 2 inverse matrix of the Jacobian given by $\partial(\tilde{\psi}_{\rm R}, \tilde{\psi}_{\rm Z})/(R,Z)_{AX}$.

When the artificial stabilization field is converged to zero (below a given tolerance), the equilibrium has been found consistently. This procedure was already shown to work well in the SPIDER code as described in [I$^+$05, IKMP09].

In figure (2)(left) the trajectory of the values of $R_{\rm ax}, Z_{\rm ax}$ is shown along the number of iterations at the first equilibrium call, with the sum of the artificial field squared $\xi_{\rm stab} = \sqrt{\tilde{\psi}^2_{\rm R} + \tilde{\psi}^2_{\rm Z}}$ on the (right) plot. For this specific case, the same plasma shown in figure (1), but run in free boundary mode, the first equilibrium converges after 10 iterations, where the tolerance has been set as $\xi_{\rm stab} < 10^{-8}$.

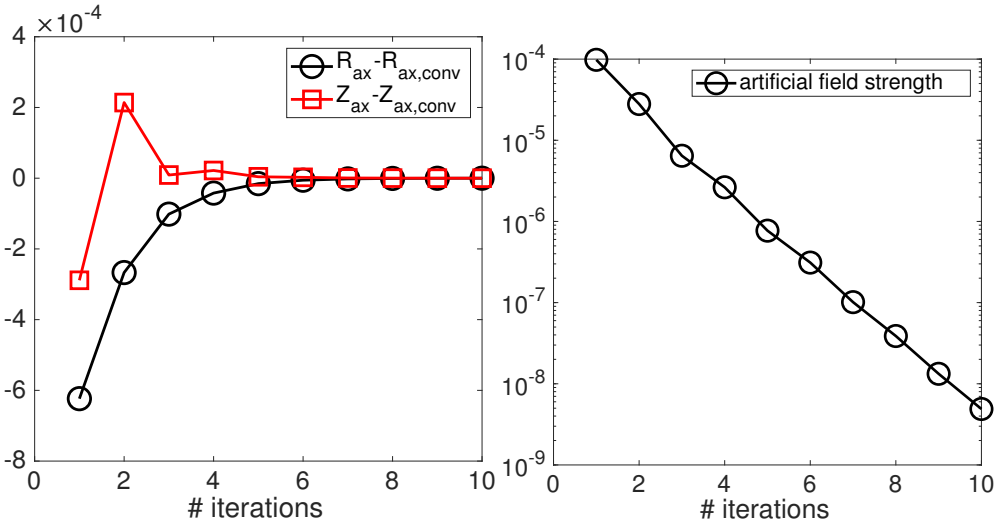

Figure 2: Convergence of the first equilibrium using the artificial field technique: (left) magnetic axis major radius $R_{\rm ax}$ and vertical position $Z_{\rm ax}$ relative to the converged value as a function of the iteration nr.; (right) strength of the artificial field $\xi_{\rm stab}$.

2.2.2 Static inverse solution at initialization

If the coil currents do not have to be strictly fixed, but can be varied a little to allow the plasma to find an equilibrium arbitrarily close to the one given as guess (for example prescribing a boundary and a magnetic axis), then this inverse mode performs this task. In this case, a global optimization problem is solved, where the cost function is given as:

$$F_{\rm gloptim} = \sigma_B \sum_b \left(\psi_b - \langle\psi_b\rangle\right)^2 + \sum_j \sigma_{I,j} \left(I_j - I_j^0\right)^2 + \sigma_{ax} \left(\left|\frac{\partial\psi}{\partial R}\right|_{ax}^2 + \left|\frac{\partial\psi}{\partial Z}\right|_{ax}^2 \right) \tag{5}$$

where $\sigma_B, \sigma_{I,j}, \sigma_{ax}$ are weight coefficients, respectively for the reference boundary points, the reference conductor currents, and the reference magnetic axis position (which does not need to coincide with the real magnetic axis). ψ_b is the actual value of the magnetic flux on the prescribed boundary points (index "b", running from 1 to N_b), and $\langle\psi_b\rangle$ is their average. I_j, I_j^0 are respectively the conductor currents and their reference values of the conductor $j = 1..N_{\rm conduc}$, and finally the last term is the amplitude of the magnetic flux gradient on the reference axis position (while it being strictly 0 on the true magnetic axis). Note that the various weight coefficients σ's do not need to have the same units (and as such similar values). However it is not difficult to identify possible normalization as a future task.

To simplify the problem characterized by the cost function (5) and make it linear, one first expresses the full flux as $\psi = \psi_{\rm plasma} + \psi_{\rm ext}$, with the former the flux produced by the plasma current density and the latter the flux produced by the external conductors. We then make the approximation that $|\partial\psi_{\rm plasma}/\partial I| \ll |\partial\psi_{\rm ext}/\partial I|$, where I is a generic conductor current. If the plasma was a non–deformable conductor, the left–hand–side of the comparison would be strictly 0. However, even with the plasma as a fluid, that approximation is still valid especially close to the actual solution.

To solve the optimization problem, one first computes analytically the derivative of the cost function with

respect to the conductor current j, which is:

$$\delta F_{\mathrm{gloptim,j}} = 2H_j$$
$$H_j = \sigma_{I,j}\left(I_j - I_j^0\right) + \sigma_B \sum_b \left[\left(\psi_b - \langle\psi_b\rangle\right)\left(G_{j,b} - \langle G_{j,b}\rangle\right)\right] + \\ + \sigma_{ax}\left(\left|\frac{\partial\psi}{\partial R}\frac{\partial G_j}{\partial R}\right|_{ax} + \left|\frac{\partial\psi}{\partial Z}\frac{\partial G_j}{\partial Z}\right|_{ax}\right) \tag{6}$$

where G_j is the Green function from the conductor j to the boundary point b or to the magnetix axis "ax".

The Newton iteration scheme in this case is the following:

$$\delta I_j = -(\mathbf{M} \times \delta F_{\mathrm{gloptim}})_j \tag{7}$$

where $\mathbf{M}$ is a matrix obtained in this way:

$$\mathbf{M} = (2X)^{-1}$$
$$X_{i,j} = \sigma_{I,i}\delta_{i,j} + \sigma_B \sum_b \left(G_{i,b} - \langle G_{i,b}\rangle\right)\left(G_{j,b} - \langle G_{j,b}\rangle\right) + \sigma_{\mathrm{ax}}\left(\frac{\partial G_i}{\partial R}\frac{\partial G_j}{\partial R} + \frac{\partial G_i}{\partial Z}\frac{\partial G_j}{\partial Z}\right)_{\mathrm{ax}} \tag{8}$$

where $\delta_{i,j}$ is the Kronecker symbol $\delta_{i,j} = 1$ if $i = j$, 0 otherwise. Since the matrix X is independent of the magnetic flux or the conductor currents, it can be pre–computed before the iterations are performed.

When the iteration scheme, equation (7), converges, the correction terms δI_j are applied to the conductor currents to find the new vacuum magnetic flux on which the plasma develops.

It is also possible to compute the coil currents from scratch, that is with null reference values. In this case, the cost function (5) is modified in that the coils term is:

$$F_{\mathrm{gloptim}} = \ldots + \sum_j \sigma_{I,j}\frac{1}{2}L_j I_j^2 + \ldots \tag{9}$$

where L_j is the self–inductance of conductor j. This makes the cost function sensible on the magnetic energy generated by each individual coil.

Finally, inspired by what has been implemented in the NICE code [Fau20], the code can also compute a set of currents, which develop a time trajectory of provided shapes, including the required loop voltage that the plasma needs to maintain its plasma current I_{p}. For this case, additionally the plasma external inductance L_{ext}, plasma current at the present time slice I_{p}, and the differential variation of the plasma boundary flux during the lapsed time $\delta\psi = V_{\mathrm{loop}}\delta t + L_{\mathrm{ext}}\delta I_{\mathrm{p}}$. The cost function is then modified by the following additional term:

$$F_{\mathrm{gloptim}} = \ldots + \lambda\left[\delta\psi - V_{\mathrm{loop}}\delta t - L_{\mathrm{ext}}\delta I_{\mathrm{p}}\right] \tag{10}$$

where λ is a Lagrange multiplier. This additional term enforces the flux balance between the two time slices, where the external flux differential created by the coils has to balance the flux loss by plasma resistance and inductance. Note that voltage limits for each coil can be given, in which case the optimal value of the new coil currents have to fall in between the two current limits given by the estimate:

$$I_{\mathrm{lim}} = I_{\mathrm{ref}} + \delta t\left[V_{\mathrm{lim}} - RI_{\mathrm{ref}}\right]/L \tag{11}$$

where "ref" means the coil current found at the previous time point, and R, L are respectively the resistance and self–inductance of the coil. These constraints maintains the time variation of the fitted coils smooth and sensible even if the actual circuit equations are not really solved.

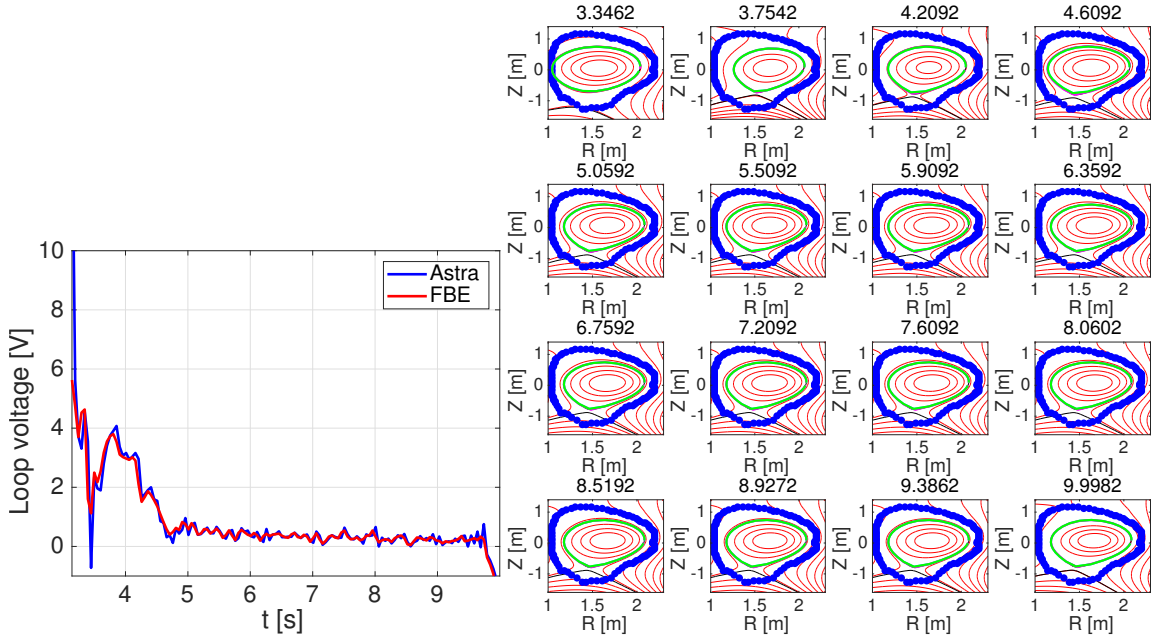

Figure 3: (left) Comparison of the loop voltage estimated in Astra to get the requested plasma current given the plasma resistivity (blue line, "Astra") and the loop voltage calculated a–posteriori from the fitted coil current evolutions, shown in figure (4) (red line); (right) comparison of the requested shapes (green) and the fitted shapes (black line, whereas the red lines are all the other ψ contour lines). The blue thick contour represents the limiter surface used in the simulation. When the plasma touches this contour, it becomes limited, otherwise it is an X-point configuration.

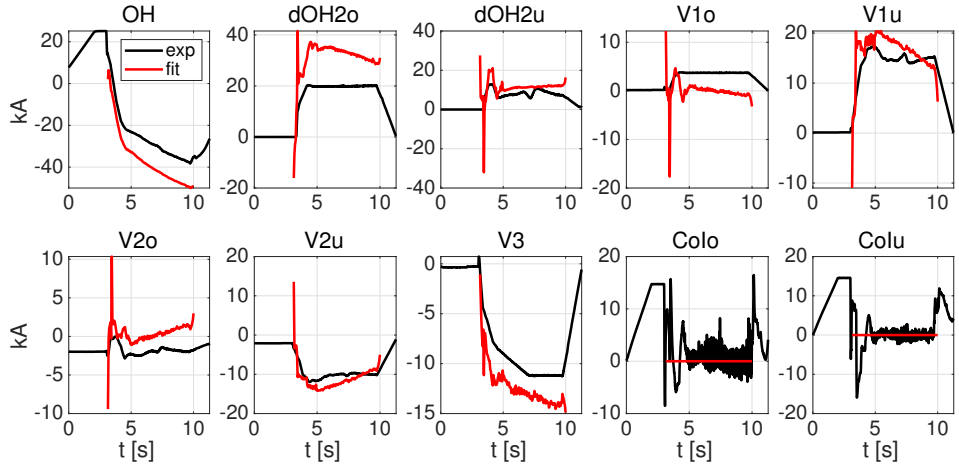

Figure 4: Comparison of the fitted coil currents "fit" (red lines) with the experimental currents "exp" (black), for the active coils of AUG: OH, dOH2o, dOH2u, V1o, V1u, V2o, V2u, V3. The position control coils Colo and Colu have not been fitted.

In figure (3) an example of dynamical coil fitting for an entire AUG discharge (#40446) is shown. The left plot shows the comparison between the loop voltage calculated from Astra (blue line) to get the desired plasma current (imposed from the experimental time trace) and the one calculated a–posteriori from the fitted coil currents evolution (red curve). The comparison shows that, as desired, the fit procedure satisfies the constraint imposed on the change of external magnetic flux, such as to balance the required loop voltage at the plasma boundary.

On the right plot, the comparison of the fitted separatrix (black) with the requested shape (green) is displayed. The fit maintains the requested shape almost to perfection.

Finally, in figure (4), the fitted coil currents (red) are compared with the experimental coil currents (black). Note that the fit procedure knows nothing about the experimental currents. For this case, the fit constant σs have been chosen to come close to the measured coil currents, but a discrepancy is expected since the fit does not know about current limits nor voltage limits (which have not been used in this case). Note also that the CoIo and CoIu currents, which are active control currents, have not been used for the fit, since these coils are only used for active control of the plasma during operation, and are not envisioned as static shaping coils for designing shapes in AUG.

2.2.3 Dynamical evolution in vacuum

For the external conductors, both active and passive, FEQIS solves circuit equations of the type:

$$L_j \frac{dI_j}{dt} + \sum_i \left[M_{i,j} \frac{dI_i}{dt} + R_{i,j} I_i \right] = V_j + (\text{plasma term})_j \tag{12}$$

with $L_j, M_{i,j}$ the self and mutual inductances, and $R_{i,j}$ the resistance matrix (allowing for complex connections of the coils). The supplied voltage to the coils is V_j, while passive conducting structures are assigned 0 external voltage input. The last term on the right–hand–side is the term that represents the effect of the magnetic field produced by the plasma onto the conducting structures.

Note that the code is also capable of changing the circuit connections (resistance matrix, inductances, and number of coils) during the time evolution, if required, which reflects the case of some devices where resistors can be switched on or off, and some coils can be switched on or off during operation. It is also to be stressed that only axisymmetric circuits and structures are represented in this code. 3D passive elements or closed loop currents that do not close toroidally cannot be taken into account except via some "effective" resistance effectively acting in the toroidal direction.

This system of 0D (in space) equations is solved in time with an implicit scheme, to ensure stability even at large time step. The only explicit term being the plasma term, thus requiring the time step being at least smaller than the typical time scale of plasma motion due to the varying conductor currents. In the case of vacuum calculations in absence of the current–carrying plasma, the "plasma term" is set to 0.

2.2.4 Dynamical evolution with plasma

After the gas is ionized at the breakdown inside the vacuum chamber, the equations (12) start to include a finite plasma term:

$$(\text{plasma term})_j = -\frac{d\Psi_j}{dt} \tag{13}$$

with Ψ_j the magnetic flux created by the plasma onto the region of conductor j.

Since the plasma flux is computed by the static GSE, the system comprising of equations (12) and GSE are iterated at fixed time slice until the sum of conductors and plasma fluxes converges. Note that this iteration scheme converges only if the plasma+coils system is in the "resistive" branch of the MHD spectrum. Alfvènic dynamics is not included in this framework.

2.3 Details on the algorithm to solve the FBGSE

Independently of the mode of operation chosen to solve the free boundary equation, a few steps are always performed to calculate the full solution. Here the details of these steps are presented.

2.3.1 Rectangular GSE solver

Given the toroidal current density distribution $j_\phi(R,Z)$ and the external flux map $\psi_{\text{ext}}(R,Z)$, the full flux is obtained by linearly overlapping the plasma flux ψ_{pl} and ψ_{ext}. The plasma contribution is obtained by solving the following 2 steps system inside the simulation domain $(R,Z) \in \Omega$ defined as Ω, whose boundary is called $\partial\Omega$:

$$\begin{aligned} \Delta^* g &= j_\phi \quad ; \quad [g]_{\partial\Omega} = 0 \\ \Delta^* \psi &= j_\phi \quad ; \quad [\psi]_{\partial\Omega} = z(g) \end{aligned} \tag{14}$$

where the boundary function $z(g)$ is obtained by performing boundary integrals of the Green function and the perpendicular gradient of g. Note that the cyclic integral, when it happens to consider self–inductance of a small segment of boundary, uses an analytical formula for the segment self–inductance as computed in [BL77]. Numerically, the pair of equations (14) are solved using the discrete sine transform method in the vertical direction as in [RPFtAUT16].

Once the plasma solution is obtained, the full flux is given by: $\psi = \psi_{\text{pl}} + \psi_{\text{ext}} + (artificial\ field\ if\ needed)$.

2.3.2 Finding the value of the magnetic axis position and the LCFS flux

Now one has the full map $\psi(R,Z)$. To find the magnetic axis, one starts from the previously found value (or initially from a guess value), and a simple "uphill" search algorithm will find the grid point with the maximum value of ψ. After this, a local 9–point exact biquadratic interpolation routine will refine the solution and find the real values of R_{mag} and Z_{mag}. In practice, upon expanding locally $\psi \approx c_1R^2Z^2 + c_2R^2Z + c_3RZ^2 + c_4RZ + c_5R^2 + c_6Z^2 + c_7R + c_8Z + c_9$, a Newton scheme is employed to find the location that satisfies $\partial\psi/\partial(R,Z) = 0$.

For the plasma boundary value, ψ_b, the algorithm is a bit more complex. At the very first calculation, the code performs a full sweep of the 2D grid, and finds all points that satisfy the condition $\left|\frac{\partial\psi}{\partial R}\right|^2 + \left|\frac{\partial\psi}{\partial Z}\right|^2 = 0$, which can be either O–points or X–points (aka null–gradient–points or NGPs). Obviously, the O–point which coincides with the magnetic axis is discarded as it cannot be the plasma boundary at the same time. Next, all NGPs that lie outside the limiter region are excluded. Conversely, all limiter points that are in the shadow of an X–point are discarded. This is done by considering the domain divided in 4 quadrants with respect to the magnetic axis. Any X–point point that appears in each quadrant defines the maximum (or minimum) side of the box in which the plasma should be contained. In this way, it is clear that the plasma LCFS cannot bypass an existing X–point on the same side (right, left, top, bottom). This is a rather crude description of the X–point shadow regions, but it is found to be working well for typical tokamak plasma configurations. Finally, all NGPs that are non–monotonically connected to the magnetic axis are also excluded. That is, if going from the NGP to the magnetic axis, there is an inversion of the magnetic flux gradient, the NGP cannot be the plasma boundary. Moreover, limiter points that are in the shadow of NGPs are also not considered. This is simply achieved by checking in which quadrant, with respect of the magnetic axis, the NGP point is, and then cutting the domain on the other side of the NGP point, with respect to the magnetic axis. This is a rather simple and crude procedure, but it works for typical tokamak equilibria.

After having removed all pathological flux grid points, what remains between limiter points and NGPs is compared in terms of the magnetic flux: the highest magnetic flux is assigned as the real plasma boundary

value. From the second iteration on, or when the dynamical calculations are performed, the full 2D sweep is not done. Instead, a sweep is done over the plasma LCFS of the previous iteration, to find (eventually) new NGPs. Note that the search algorithm uses again a 9–points exact biquadratic interpolant, where the null–gradient condition is obtained via a local Newton method solution.

When the poloidal flux value for the plasma boundary is found, an algorithm is employed to define a set of points that describe this boundary in polar coordinates (ψ, θ) (Carthesian θ) which is then used in prescribed boundary mode to evaluate the internal flux surface with more accuracy and compute the flux–surface–average geometric quantities eventually needed by the transport code that embeds FEQIS. This algorithm moves along the angle θ, and for each angle, moves along the ray from the magnetic axis outwards, in steps of $ds = \sqrt{(dr\cos\theta)^2 + (dz\sin\theta)^2}$, with dr, dz the grid resolution steps in radial and vertical direction.

2.3.3 Deploying the new map of the current density

Once the new magnetic axis and LCFS flux values are found, the flux ψ is normalized between 0 (axis) and 1 (boundary). Next, a sweep algorithm, which starts from the closest grid point to the magnetic axis, checks all grid points moving outside in spiraling fashion, until either the boundary flux is found, or the NGP or limiter point is found. Points close to the boundary, but in the exterior vacuum region, are also stored as "ghost" points, which will be discussed briefly later on. The plasma current density is assigned to the interior points simply by interpolating the values of P', FF' from their original ψ normalized grid, onto the free–boundary solution normalized ψ.

Since the boundary can cut in between grid points in different ways, an algorithm is used to assign a current density to the exterior "ghost" points, to mimic the fact that the plasma partially occupies cells. Suppose that the boundary would cut between grid points $1G$ and $2G$, where "1" is at the left of "G", and "2" is under "G". Let us call t_1 and t_2 the normalized distances between $1B_{1G}$ and $2B_{2G}$, where B_{1G}, B_{2G} are respectively the location of the intersection between the real boundary and the grid points connection grid lines. Let us also call the values of the current densities at B_{1G}, B_{2G} as j_{1G} and j_{2G}. Then the value of the assigned current density on the ghost external point G is: $j_G = t_1 j_{1G} + t_2 j_{2G} - t_1 t_2 (j_{1G} + j_{2G})/2$.. Then, we also define $I_G = t_1 + t_2 - t_1 t_2$, whereas $I_G = 1$ for interior points. The current is then smoothed by employing a second order Shapiro filter for each grid point (l, k): $j_{\text{corrected}}(l,k) = I_G(l,k) 0.5\,[j(l,k) + 0.25(j(l+1,k) + j(l-1,k) + j(l,k+1) + j(l,k-1))]$. This smoothing avoids extreme current profile gradients caused by a coarse–gridding of the 1D profiles. It can be seen that the formula for the ghost points satisfies all the properties of the current density whenever the boundary intersects an actual grid point or when either t_1, t_2 are 0.

This way of distributing the edge current density on external ghost points makes the code physically sensitive to the boundary moving in between grid points, which is one goal of this method. The accuracy of this method is however low order (first order accuracy), whereas other methods can be found in the literature that reach second order accuracy [FMS92]. These more sophisticated methods could be implemented and tested in the future.

2.3.4 Coupling with the 1D current diffusion equation

The 2D GSE solution provides only the geometry of the flux surfaces, both for the nested closed field line region (plasma core) and the external region which is characterized by open field lines and the presence of the external conductors. In the plasma core, from the side of the transport solver, a 1D current diffusion equation (CDE) is usually solved for, to provide the 1D profile of the poloidal magnetic flux ψ as a function of the underlying radial coordinate, which usually is the toroidal magnetic flux Φ. As such, the 1D CDE provides $\psi_{1D}(\Phi)$, whereas the 2D FBGSE provides $\psi_{2D}(R, Z)$. From the point of view of the code evolution, the two fluxes are independent of each other. However, at the interface (the LCFS), the two fluxes must have the same

value:

$$\psi_{1D}(LCFS) = \psi_{2D}(LCFS) \tag{15}$$

This condition has to be forced from the side of the plasma core. That is, equation (15) has to be seen as a definition of $\psi_{1D}(LCFS)$, that is the boundary condition for the CDE.

The problem is then to find an expression of $\psi_{2D}(LCFS)$, that contains implicitly $\psi_{1D}(LCFS)$, since equation (15), when taken as an explicit definition, is extremely unstable during the time evolution. To solve this issue we follow [KL93] and employ the following exact relation:

$$\psi_{1D}(LCFS) = \langle \psi_{\text{ext}} \rangle_b + \langle \psi_{\text{plasma}} \rangle_b \tag{16}$$

where $\langle ... \rangle_b$ denotes averaging over the plasma boundary (LCFS), and the second term on the right hand side represents the plasma contribution to the boundary flux. This contribution can be represented as $\langle \psi_{\text{plasma}} \rangle_b = L_{\text{ext}} I_{\text{p}}$, with L_{ext} the external inductance of the plasma, and I_{p} the plasma current. The value of the external inductance is calculated via a double integral over the boundary using the Green function: $L_{\text{ext}} = \frac{1}{2\pi\mu_0 I_{\text{p}}} \langle \oint \frac{1}{R} G |\nabla\psi| dl \rangle_b$. On the other hand, the plasma current is expressed through the boundary gradient of the poloidal flux: $I_{\text{p}} = G(\partial\psi/\partial\rho)_b$, with the geometrical parameter G given by:

$$G = \frac{1}{4\pi^2\mu_0} \frac{dV}{d\rho} \left\langle \frac{|\nabla\rho|^2}{R^2} \right\rangle \tag{17}$$

with V the local plasma surface volume and ρ a generic radial coordinate (in ASTRA it is defined as $\rho = \sqrt{\Phi/(\pi B_0)}$ with Φ the toroidal magnetic flux and B_0 the reference toroidal magnetic field). In the following, we omit the "1D" pedix of the flux ψ calculated in the current diffusion equation except when said otherwise.

Physically, condition (16) simply says that the total flux on the plasma boundary is the sum of the vacuum flux created by external conductors plus the flux generated by the plasma itself. Substituting equation (16) in (15) we find our implicit boundary condition for the CDE:

$$\psi_b = \langle \psi_{\text{ext}} \rangle_b + L_{ext} G \left| \frac{\partial\psi}{\partial\rho} \right|_b \tag{18}$$

where the external flux produced by the coils and the conducting structures ψ_{ext} acts effectively as a source of boundary flux. This implicit (and thus fully stable) boundary condition determines simultaneously the values of ψ_b and I_{p} and lead to the full closure of the dynamical problem.

2.3.5 Speeding up the code

As mentioned in the introduction as a well known fact, the FBGSE system is non–linear, because the plasma current density is remapped from the flux surfaces ψ of the old iteration, to the new iteration result. As such, one single calculation does not suffice. Moreover, the kinetic profiles themselves need to be iteratively re–adapted on the new flux surfaces. This requires performing nested iteration cycles if the numerical scheme does not solve the entire plasma system in one single place (e.g. transport solver + equilibrium solver usually solve on different grids). Performing the full iteration scheme may be rather time–consuming, especially if parallelization of the individual elements is not available. For this reason, in FEQIS the user has the option to switch off any sort of iteration scheme at fixed time steps, and instead use the time variable as effective "iteration parameter". This is justified if the time step is lower than the typical time scales like the confinement time, or the current density/plasma motion (resistive time), or the conductor currents (L/R) time scale.

Moreover, the calculation of the conductor currents is decoupled from the plasma term itself. That is, in equation (12), the plasma term, equation (13), is "frozen" in between two consecutive GSE calls, where the time derivative is correctly computed using the equilibrium calls time difference. In this way, while the vacuum field is effectively changing following the conductor currents evolution, the plasma itself is only updated every now and then. This is particularly advantageous in steady–state phases with no particularly strong perturbations. The algorithm is devised to call the GSE when relative changes in several parameters (defined by the user) are observed, e.g. plasma β and l_i, or the plasma position $(R, Z)_{AX}$. The non–linear iterations can be switched on at any time during the code run, thus allowing the user to accelerate or slow down the calculation depending on the accuracy needed. For example, the non-linear iterations could be switched back on if a vertical displacement event (VDE) is detected (check on the vertical position variation). Presently, no specific criterion is included in the code, whereas this has to be defined by the user itself. In the simulations shown later, the criterion used to define at which time the GSE solver is called (non–linear iterations are permanently switched off) is described below. First, the time between calls can only vary between a minimum which is the same as the circuit equations τ_{cirq}, and a maximum which we define as $5\tau_{\mathrm{cirq}}$. Starting from the minimum, the time between calls is increased by 10% at every time step if $\varepsilon < 1\%$, where $\varepsilon = (|Z - Z_0| + |R - R_0|)/a$, and the magnetic axis position values R, Z are the new evaluation and R_0, Z_0 is the old evaluation. a is the plasma minor radius. If the error $\varepsilon > 1\%$, the interval between calls is reduced by 20%.

Finally, the code can be run with the minimal grid resolution compatible with still accurate results, which in the simulations shown later, is 65x65 grid points, and the solution region is minimally surrounding the limiter area. A comparison of the results obtained using a 65x65 or a 129x129 grid will be shown later in figure (11).

3 Application in Fenix and benchmark against SPIDER

The FEQIS code has been coupled to the ASTRA transport solver [PY91, FAC+13], and used as the dynamical FBGSE solver to carry out full–discharge simulations in the flight simulator Fenix [FJT+22]. Here we apply this integrated modeling tool to ASDEX Upgrade discharge #40405, a H–mode discharge characterized by a short flat-top and long ramp–down. ASTRA is also coupled to the free boundary GSE solver SPIDER [IKMP09], which is used here to benchmark the new code FEQIS.

In the set of figure 5, figure 6, and figure 7, the result of the benchmark on the full–discharge evolution is provided. As it can be seen from the three plots, the agreement between the new code FEQIS and the established SPIDER code is excellent. A small discrepancy can be seen randomly around each trace, which is expected since the codes use different algorithms. However in FEQIS a higher sensitivity of the plasma shape on details of the edge pressure gradient is observed, leading to a slightly larger plasma Shafranov shift. This results in a visible, albeit small, systematic difference in the innermost plasma boundary major radius R_{in} and the plasma vertical top position Z_{top}.

3.1 Comparison between different levels of iterations accuracy

Before concluding, three runs have been carried out, where the results are compared when running FEQIS with full non–linear iterations at the same time step (slower mode), without non–linear iterations but calling the GSE solver at each time step, and finally when sparsely calling the GSE solver depending on the background variation of plasma parameters.

The comparison is displayed in figures (8, 9, 10).

It can be seen that there is practically no difference between the various runs (the basic time step used here is 0.2 ms). However, the run with full non–linear iterations is much slower, requiring around 4 minutes to be performed for this short time window of 2.5 s of discharge, whereas the other two modes take respectively

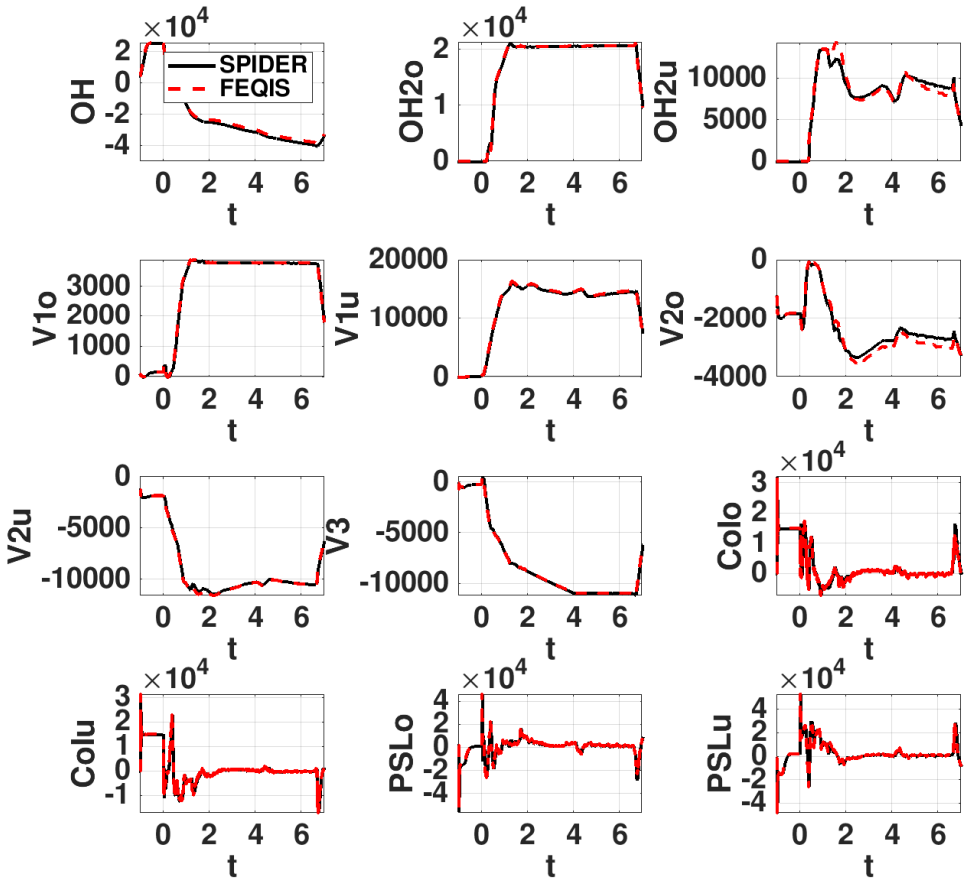

Figure 5: Time traces of the various conductor currents, all given in units of A/turn, as a function of the time along the discharge, where $t = 0$ marks the start of the breakdown plasma initiation and $t < 0$ is the vacuum phase. The code results using SPIDER are in black, whereas the code results using FEQIS are in red.

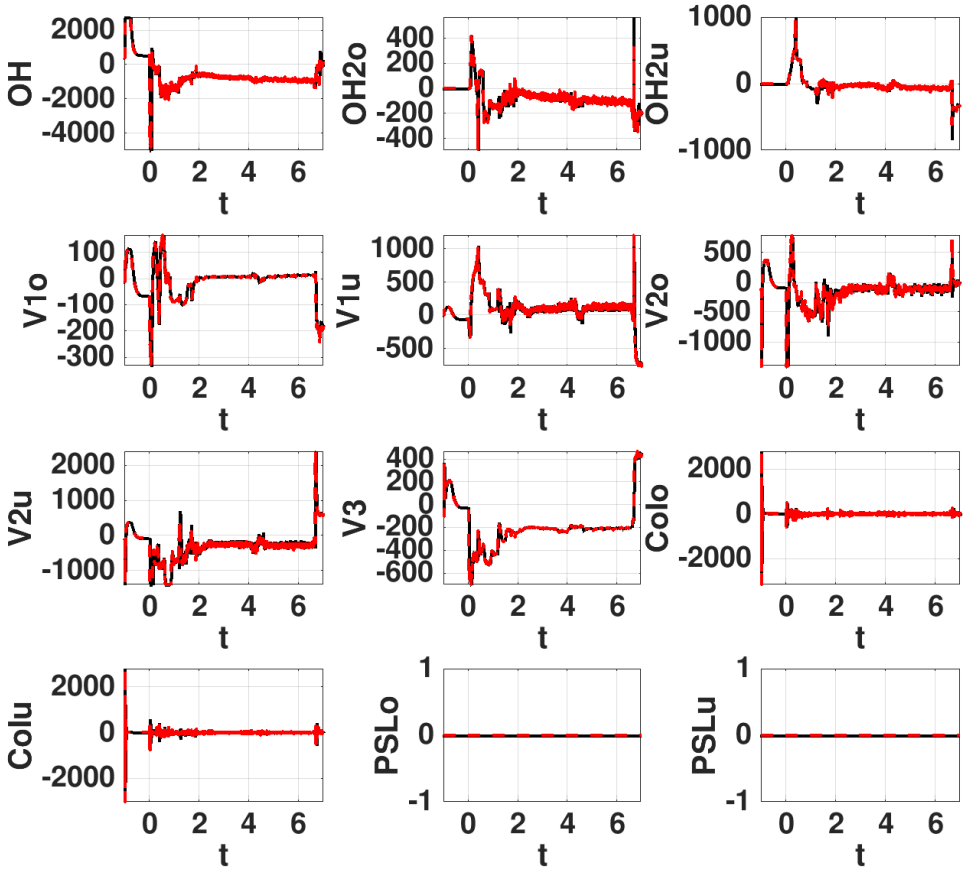

Figure 6: Time traces of the voltage applied to each individual conductor. The voltage is given in units of V. For the last two coils PSLo and PSLu, which are passive stabilizing coils, no external voltage is supplied. Color coding is the same as in the previous figure.

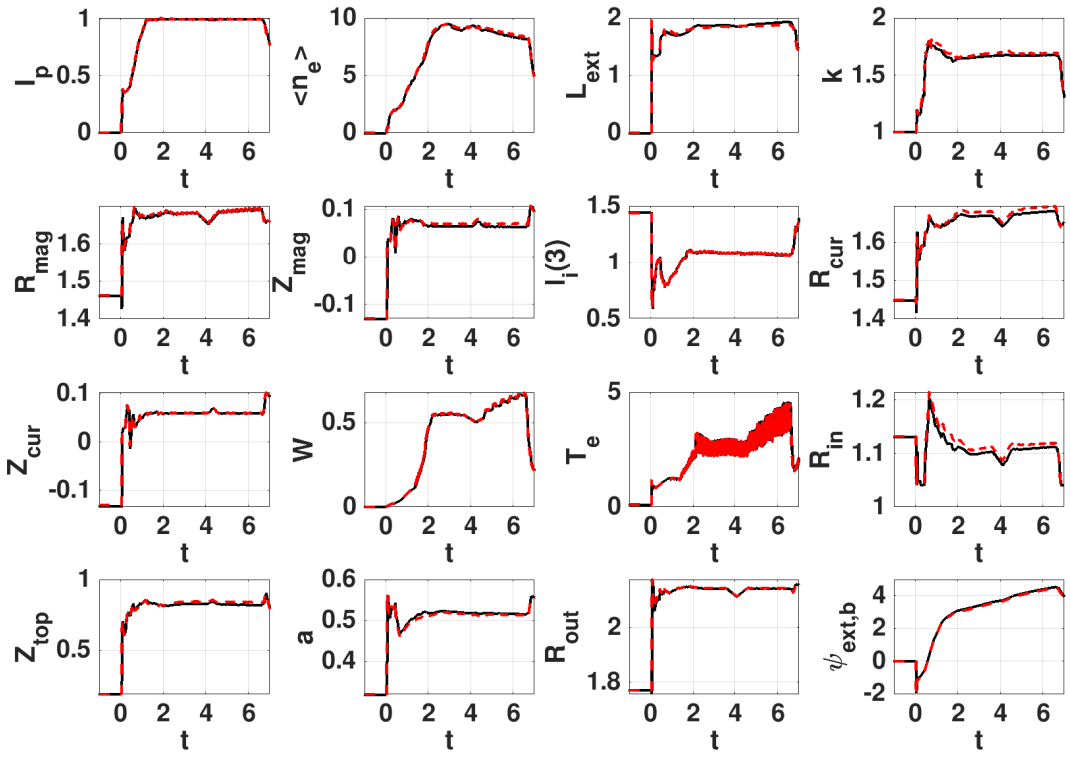

Figure 7: Time traces of various quantities: plasma current I_p [MA], line averaged density $\langle n_\mathrm{e} \rangle$ in $10^{19} m^{-3}$, plasma external inductance L_ext normalized to $2\mu_0 R$, plasma elongation k, outer strike point vertical position (o.s.p.) in [m], inner strike point vertical position (i.s.p.) in [m], internal inductance $l_i(3)$, current centroid major radius R_cur, and vertical position Z_cur, plasma energy W in [MJ], central electron temperature T_e [keV], innermost LCFS major radius R_in [m], top LCFS vertical position Z_top [m], minor radius a [m], outermost LCFS major radius R_out, vacuum poloidal flux on the plasma boundary $\psi_\mathrm{ext,b}$. Color coding is the same as in the previous figure.

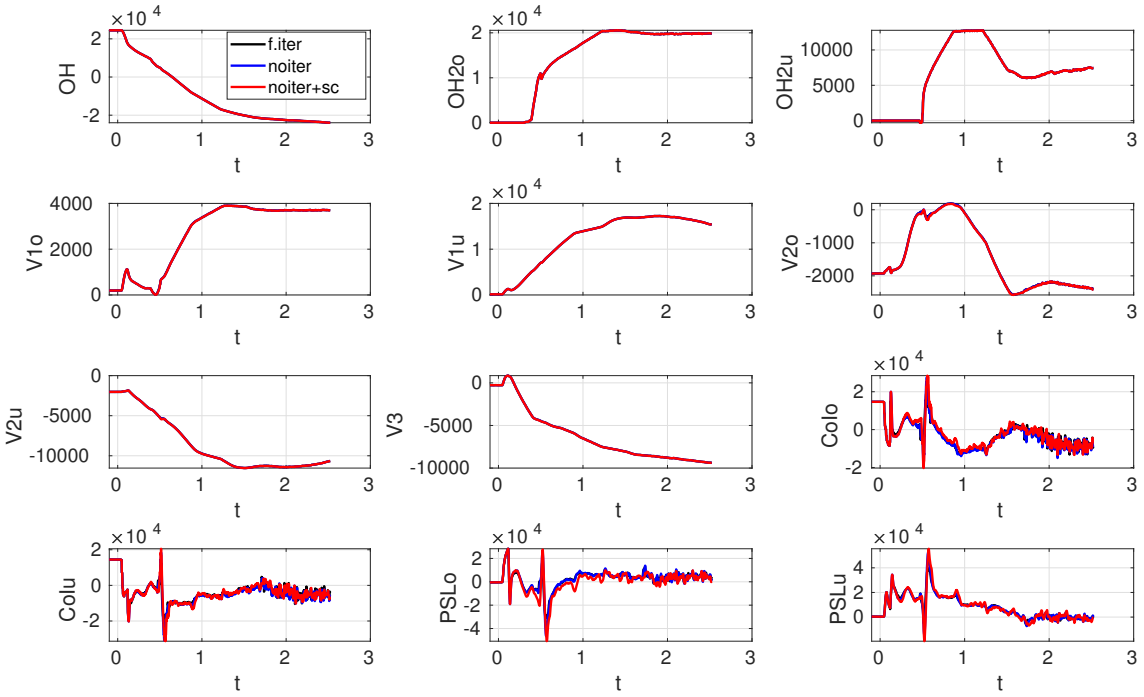

Figure 8: Comparison of time traces when running FEQIS with different approximations. "f.iter": full non–linear iterations. "noiter": only 1 call per time step, at all time steps. "noiter+sc": only 1 call per time step, but the GSE solver is called only if the plasma is changing in time depending on the rate of change. The time traces are all the active and passive coil currents in units of [A].

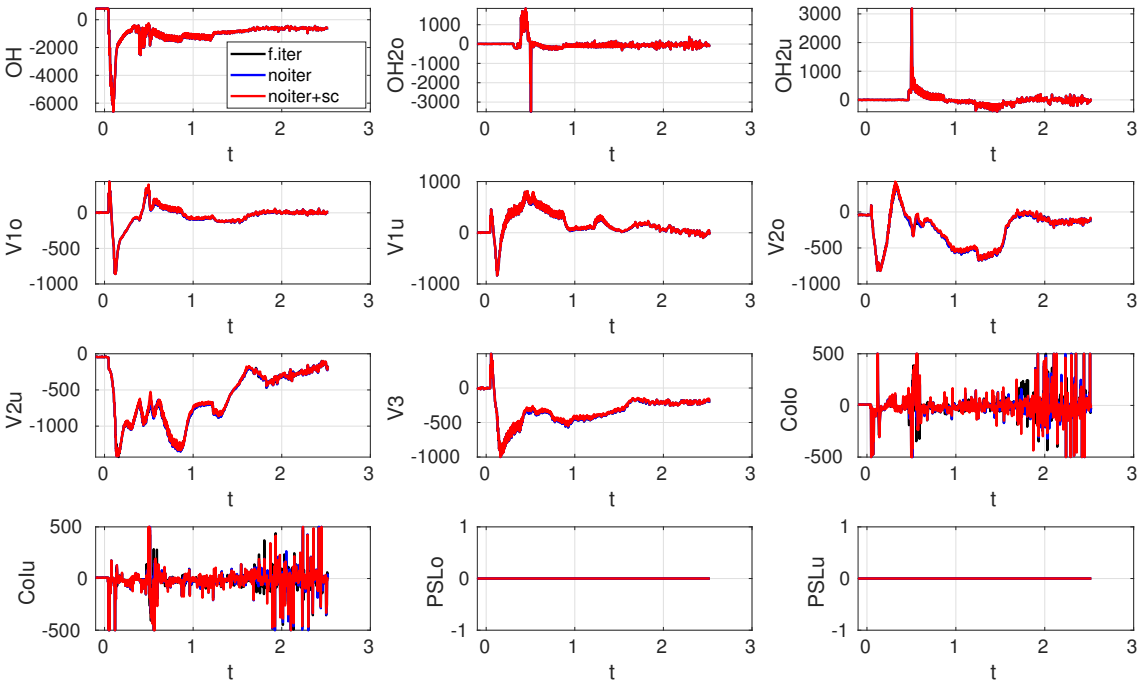

Figure 9: Color coding is the same as in the previous figure. Here the time traces are the voltages in [V] applied to the active coils (PSLo and PSLu are passive coils).

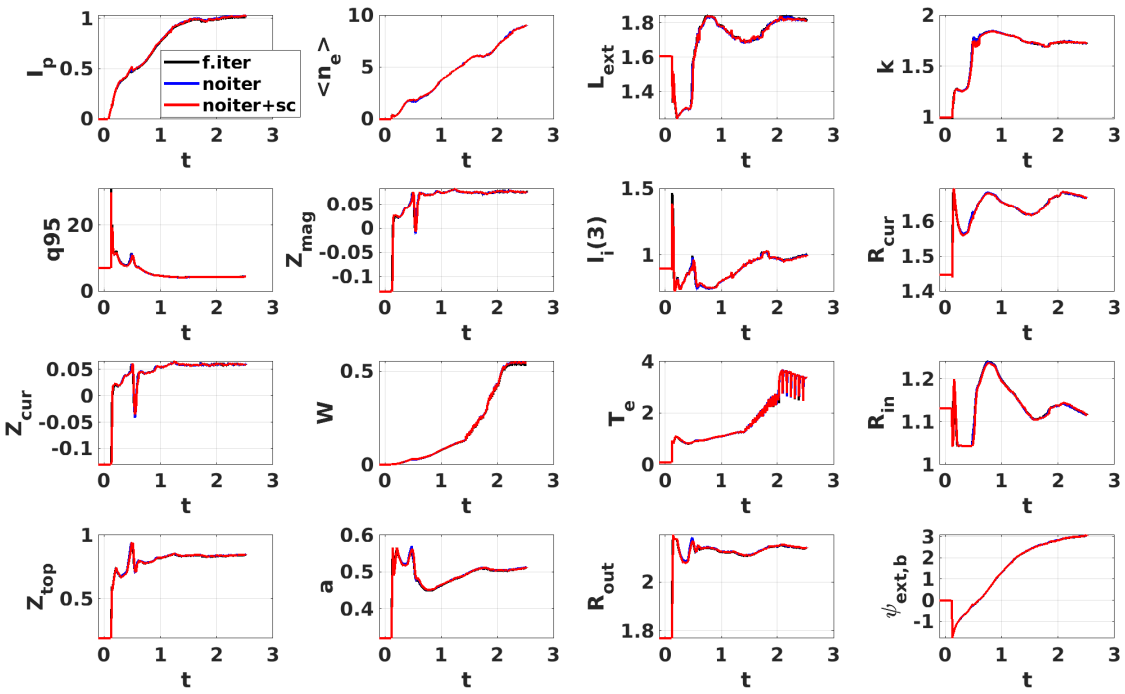

Figure 10: Color coding is the same as in the previous figure. Here the time traces are: plasma current I_{p} [MA], line averaged density $\langle n_{\mathrm{e}} \rangle$ in $10^{19} m^{-3}$, plasma external inductance L_{ext} normalized to $2\mu_0 R$, plasma elongation k, q_{95}, magnetic axis vertical position Z_{mag}, internal inductance $l_i(3)$, current centroid major radius R_{cur}, and vertical position Z_{cur}, plasma energy W in [MJ], central electron temperature T_{e} [keV], innermost LCFS major radius R_{in} [m], top LCFS vertical position Z_{top} [m], minor radius a [m], outermost LCFS major radius R_{out}, vacuum poloidal flux on the plasma boundary $\psi_{\mathrm{ext,b}}$. Color coding is the same as in the previous figure.

about 30 s when calling the GSE at every time step and about 20 s when calling it sparsely depending on the steadiness of the plasma. Notice that the sparse calls could be tailored to follow fast events and be more relaxed during quiet phases, but the precise criterion is not given as part of the code.

Finally, a comparison using 65x65 or 129x129 grid is presented in figure(11). Notably the kinetic quantities and most of the geometric quantities do not deviate by reducing the resolution. The only exception is the coil current that is modified a bit (around $\sim 15\%$) is the OH2u coil current. This coil is used for strike–point control, as such it is more sensitive to the grid resolution which impacts the accuracy with which the separatrix legs and their intersection points with the divertor targets are obtained.

4 Conclusions

In this work, a new dynamical Grad–Shafranov and circuit equation solver FEQIS is presented. This code primary scope is to do forward modeling of the plasma equilibrium evolution inside predictive modeling and particularly inside the flight simulator framework. Its various modes of operation and details of the algorithms employed to solve specific aspects of the free–boundary problem are presented.

A comparison with the SPIDER GSE solver is carried out inside the flight simulator Fenix framework, running a full–discharge prediction for an existing H–mode from the ASDEX Upgrade. The agreement between FEQIS and SPIDER is excellent and poses the basis for further developments of FEQIS. In particular, pushing the speed of the code will be the main direction going forward, whereas as of now FEQIS and SPIDER have similar computational speed when both are run with rectangular grid description. Moreover, ferro–magnetic materials will be included via the magnetization currents method.

Acknowledgments

This work has strongly benefited from discussions with various Colleagues who are experts in this field: Dr. O. Maj (IPP Garching); Dr. M. Mattei (ENEA, CREATE Consortium, University of Naples).

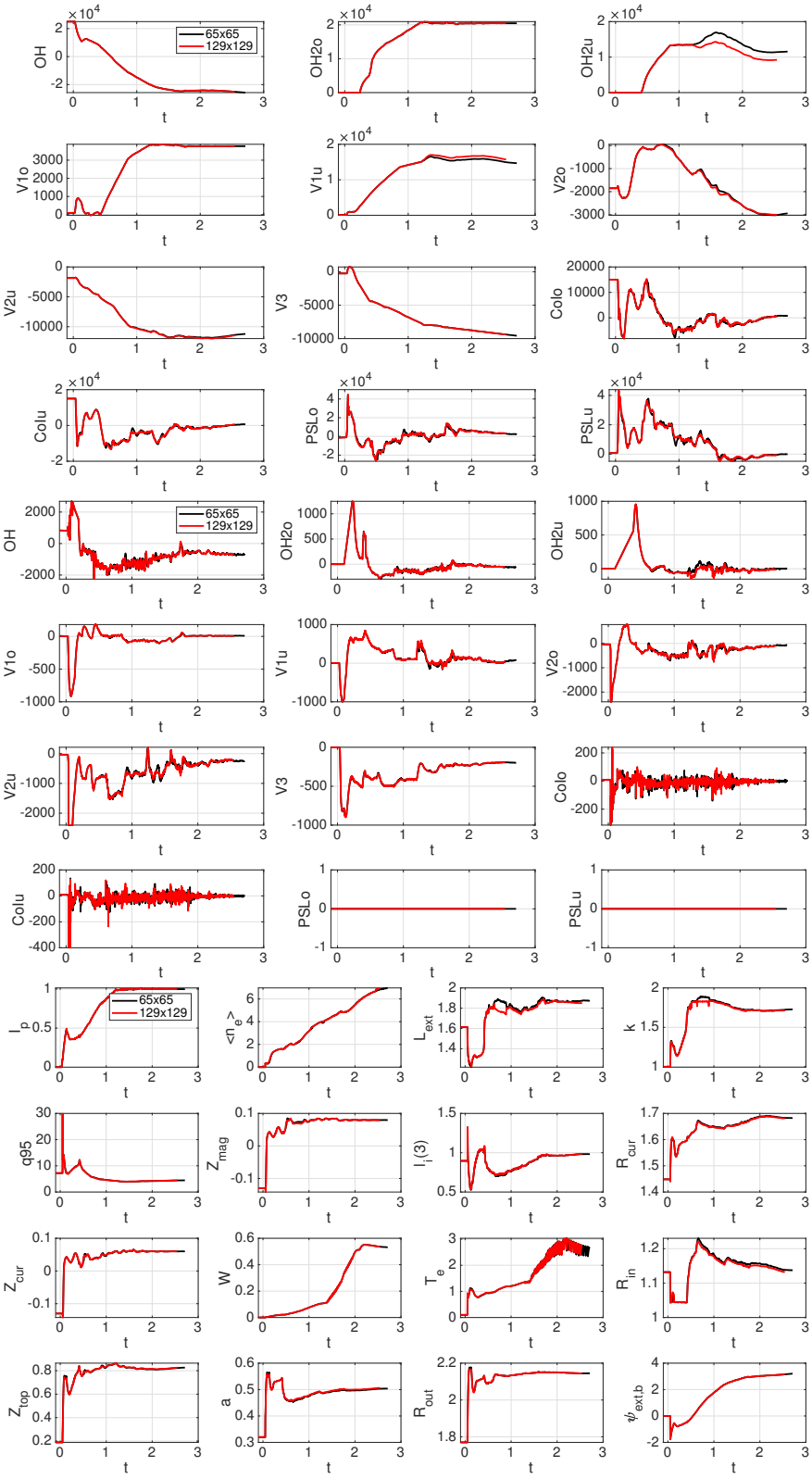

Figure 11: Same set as in figures (8,9,10), but for a comparison using a rectangular grid of 65x65 (black lines) or of 129x129 (red lines).

References

[AAM15] R. Albanese, R. Ambrosino, and M. Mattei, CREATE-NL+: A robust control-oriented free boundary dynamic plasma equilibrium solver, *Fusion Engineering and Design* **96-97** (2015), 664–667. doi:10.1016/j.fusengdes.2015.06.162.

[BL77] G. Becker and K. Lackner, Free-boundary equilibrium computations for strongly elongated Belt Pinch Plasmas, *Nucl. Fusion* **17** (1977), 903.

[BLF84] J. Blum and J. Le Foll, Plasma equilibrium evolution at the resistive diffusion timescale, *Computer Physics Reports* **1** no. 7 (1984), 465–494. doi:10.1016/0167-7977(84)90013-3.

[DFB+22] J. Degrave, F. Felici, J. Buchli, M. Neunert, B. Tracey, F. Carpanese, T. Ewalds, R. Hafner, A. Abdolmaleki, D. de las Casas, and others, Magnetic control of tokamak plasmas through deep reinforcement learning, *Nature* **602** (2022), 414–419. doi:10.1038/s41586-021-04301-9.

[ELSV24] H. C. Elman, J. Liang, and T. Sánchez-Vizuet, Multilevel Monte Carlo methods for the Grad-Shafranov free boundary problem, *Computer Physics Communications* **298** (2024), 109099. doi:10.1016/j.cpc.2024.109099.

[FAC+13] E. Fable, C. Angioni, F. J. Casson, D. Told, A. A. Ivanov, F. Jenko, R. M. McDermott, S. Y. Medvedev, G. V. Pereverzev, F. Ryter, and others, Novel free-boundary equilibrium and transport solver with theory-based models and its validation against ASDEX upgrade current ramp scenarios, *Plasma Phys. Contr. Fusion* **55** (2013), 124028. doi:10.1088/0741-3335/55/12/124028.

[FJT+22] E. Fable, F. Janky, W. Treutterer, M. Englberger, R. Schramm, M. Muraca, C. Angioni, O. Kudlacek, E. Poli, M. Reich, and others, The modeling of a tokamak plasma discharge, from first principles to a flight simulator, *Plasma Phys. Contr. Fusion* **64** (2022), 044002. doi:10.1088/1361-6587/ac466b.

[Fau20] B. Faugeras, An overview of the numerical methods for tokamak plasma equilibrium computation implemented in the NICE code, *Fus. Eng. Design* **160** (2020), 112020. doi:10.1016/j.fusengdes.2020.112020.

[FMS92] B. Fornberg and R. Meyer-Spasche, A finite difference procedure for a class of free boundary problems, *Journal of Computational Physics* **102** no. 1 (1992), 72–77. doi:10.1016/S0021-9991(05)80006-3.

[GL04] P. A. Gourdain and J. N. Leboeuf, Contour dynamics method for solving the Grad–Shafranov equation with applications to high beta equilibria, *Physics of Plasmas* **11** no. 9 (2004), 4372–4381. doi:10.1063/1.1776174.

[HSB+24] C. Hansen, I. Stewart, D. Burgess, M. Pharr, S. Guizzo, F. Logak, A. Nelson, and C. Paz-Soldan, TokaMaker: An open-source time-dependent Grad-Shafranov tool for the design and modeling of axisymmetric fusion devices, *Computer Physics Communications* **298** (2024), 109111. doi:10.1016/j.cpc.2024.109111.

[HBB+15] H. Heumann, J. Blum, C. Boulbe, B. Faugeras, G. Selig, J.-M. Ané, S. Brémond, V. Grandgirard, P. Hertout, and E. Nardon, Quasi-static free-boundary equilibrium of toroidal plasma with CEDRES++: Computational methods and applications, *Journal of Plasma Physics* **81** no. 3 (2015), 905810301. doi:10.1017/S0022377814001251.

[HS14] E. C. Howell and C. R. Sovinec, Solving the Grad–Shafranov equation with spectral elements, *Computer Physics Communications* **185** no. 5 (2014), 1415–1421. doi:10.1016/j.cpc.2014.02.008.

[I+05] A. A. Ivanov and others, *32nd EPS Conf. on Plasma Physics* **29C** (2005), 5.063.

[IKMP09] A. A. Ivanov, R. Khayrutdinov, S. Medvedev, and Y. Poshekhonov, The SPIDER code - solution of direct and inverse problems for free boundary tokamak plasma equilibrium, *Keldysh Institute preprints* **39** (2009), 24.

[JKG+24] B. Jang, A. A. Kaptanoglu, R. Gaur, S. Pan, M. Landreman, and W. Dorland, Grad–Shafranov equilibria via data-free physics informed neural networks, *Physics of Plasmas* **31** no. 3 (2024), 032510. doi:10.1063/5.0188634.

[JFET21] F. Janky, E. Fable, M. Englberger, and W. Treutterer, Validation of the Fenix ASDEX Upgrade flight simulator, *Fusion Engineering and Design* **163** (2021), 112126. doi:10.1016/j.fusengdes.2020.112126.

[Jeo15] Y. M. Jeon, Development of a free boundary tokamak equilibrium solver (TES) for advanced study of tokamak equilibria, *Journal of the Korean Physical Society* **67** (2015), 843–853. doi:10.3938/jkps.67.843.

[KL93] R. R. Khayrutdinov and V. E. Lukash, Studies of plasma equilibrium and transport in a tokamak fusion device with the inverse-variable technique, *Journal of Computational Physics* **109** no. 2 (1993), 193–201. doi:10.1006/jcph.1993.1211.

[Lac76] K. Lackner, Computation of ideal MHD equilibria, *Computer Physics Communications* **12** no. 1 (1976), 33–44. doi:10.1016/0010-4655(76)90008-4.

[MAA+24] J. McClenaghan, C. Akçay, T. B. Amara, X. Sun, S. Madireddy, L. L. Lao, S. E. Kruger, and O. M. Meneghini, Augmenting machine learning of Grad–Shafranov equilibrium reconstruction with Green's functions, *Physics of Plasmas* **31** no. 8 (2024), 082507. doi:10.1063/5.0213625.

[MFA+23] M. Muraca, E. Fable, C. Angioni, T. Luda, P. David, H. Zohm, A. Di Siena, and the ASDEX Upgrade Team, Reduced transport models for a tokamak flight simulator, *Plasma Phys. Contr. Fusion* **65** (2023), 035007. doi:10.1088/1361-6587/acb2c6.

[PKF16] A. Palha, B. Koren, and F. Felici, A mimetic spectral element solver for the Grad–Shafranov equation, *Journal of Computational Physics* **316** (2016), 63–93. doi:10.1016/j.jcp.2016.04.002.

[PCF+13] A. Pataki, A. J. Cerfon, J. P. Freidberg, L. Greengard, and M. O'Neil, A fast, high-order solver for the Grad–Shafranov equation, *Journal of Computational Physics* **243** (2013), 28–45. doi:10.1016/j.jcp.2013.02.045.

[PY91] G. V. Pereverzev and P. N. Yushmanov, *IPP Report* **5/42** (1991).

[RPFtAUT16] M. Rampp, R. Preuss, R. Fischer, and the ASDEX Upgrade Team, GPEC: A real-time–capable tokamak equilibrium code, *Fusion Science and Technology* **70** no. 1 (2016), 1–13. doi:10.13182/FST15-154.

[RCRF16] L. Ricketson, A. Cerfon, M. Rachh, and J. Freidberg, Accurate derivative evaluation for any Grad–Shafranov solver, *Journal of Computational Physics* **305** (2016), 744–757. doi:10.1016/j.jcp.2015.11.015.

[Sha60] V. D. Shafranov, Equilibrium of a plasma toroid in a magnetic field, *Sov. Phys. - JETP* **10** (1960), 775.

[WSRS24] Z. Wang, X. Song, T. Rafiq, and E. Schuster, Neural-network-based free-boundary equilibrium solver to enable fast scenario simulations, *IEEE Transactions on Plasma Science* **52** no. 9 (2024), 4147–4153. doi:10.1109/TPS.2024.3375284.

[WDF+24] C. Wu, P. David, E. Fable, D. Frattolillo, L. E. Di Grazia, M. Mattei, M. Siccinio, W. Treutterer, and H. Zohm, Architecture design and internal implementation of a universal coupling between controllers and physics in a tokamak flight simulator, *Fusion Science and Technology* **80** no. 6 (2024), 766–771. doi:10.1080/15361055.2023.2234741.

Vol. 1, No. 4 (2025)

Open Plasma Science

Letter

Reactive Molecular Dynamics approach to PFAS plasma oxidation in water

Axel Richard[1,2], Pascal Brault[*1,2], Nicolas Froloff[1], Olivier Aubry[1], Dunpin Hong[1], and Hervé Rabat[1]

[1]GREMI, Université d'Orléans, CNRS; 14 rue d'Issoudun, F-45067 Orléans, France
[2]MS4ALL; 1 avenue du champ de Mars, F-45100 Orléans, France

History
Received May 27, 2025
Revised July 23, 2025
Accepted July 24, 2025
Published September 1, 2025

Identifiers
DOI 10.46298/ops.15754
HAL hal-05085555
ArXiv 2505.21031
Zenodo -

Supplementary Material
-

Abstract

This work establishes a protocol to study via Molecular Dynamics simulation the degradation of Per- and Polyfluoroalkyl Substances (PFAS) in water by hydroxyl radical. To achieve this, Molecular Dynamics simulations are carried out, using ReaxFF reactive interaction potential. Simulations are carried out under a temperature ramp for determining all possible products. Using this methodology, reaction pathways of perfluorooctanoic acid (PFOA) and perfluorooctanesulfonic acid (PFOS) are identified.

Keywords— Molecular Dynamics, simulation, reactive potential, ReaxFF, PFAS, non-thermal plasma, atmospheric plasma

* Corresponding author: pascal.brault@ms4all.eu; pascal.brault@cnrs.fr

Cite as: Axel Richard *et al.*, Reactive Molecular Dynamics approach to PFAS plasma oxidation in water, *Open Plasma Science* 1, 4 (2025), doi: 10.46298/ops.15754

1 Introduction

PFAS are fluorinated organic molecules characterized by their carbon chain saturated with fluorine instead of the usual hydrogen atoms. These molecules are widely used in industry and cosmetics, and have numerous applications in everyday products such as non-stick coatings for kitchen utensils [BAK+23]. However, numerous studies on their health impact classify them as potentially carcinogenic [AOG24] and reprotoxic [CYM+23].

Moreover, the carbon-fluorine bond in these molecules is very strong (> 5 eV), leading to a very low degradation rate, earning them the nickname "forever pollutants." Combined with their toxicity, this longevity places them at the center of numerous environmental regulations, particularly on drinking water with the European directive 2020/2184 [eud20], which already lists 20 PFAS to monitor and treat if their concentration exceeds certain thresholds.

Numerous experimental methods are attempted to study PFAS degradation [AISH23] such as non-thermal plasma at atmospheric pressure [SFB+19] or ozonation [LSC+22]. The common feature of advanced oxidation processes, including non-thermal plasma at atmospheric pressure, is the availability of the hydroxyl radical $HO^\bullet$ in water, which is recognized as a primary oxidant in [LVG10, WX12]. Despite availability of these experiments, there is a need for predicting the degradation products, pathways and rates of the very large number of PFAS, estimated above 14,000 [AGGH+24].

Since the basic mechanism of pollutant molecule degradation is a reactive process at molecular scale, Molecular Dynamics (MD) simulation is relevant for predicting degradation products. Molecular Dynamics simulations have benefited from the advent of a now popular reactive forcefield: reaxFF [vDDLA01, SHI+16]. For describing PFAS, a relevant reaxFF forcefield, able to correctly describe carbon - carbon and carbon - fluorine bonds [SSNA+13], is available. This potential has also been recently validated on a PFAS sonolysis study [dSHK+23].

In the present study, MD simulations were carried out with a temperature ramping between 300 and 5300 K. It allows to determine the temperature domains for C–C and C–F bond breaking, as well as identifying all possible products up to CO_2 conversion under action of $HO^\bullet$. It should be noticed that this work is not corresponding to a specific process, but it is proposing a methodological tool for finding energetic requirements for PFAS degradation. It is applied to the most known PFAS, say perfluorooctanoic acid (PFOA, $C_8HF_{15}O_2$) and Perfluorosulfonic acid (PFOS, $C_8HF_{17}O_3S$). Figure 1 displays the form of these two molecules.

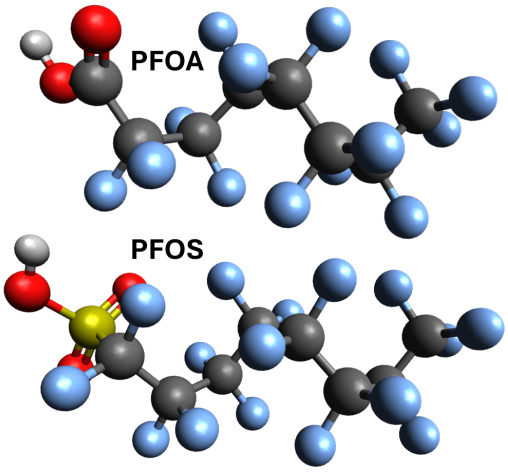

Figure 1: Drawing of PFOA and PFOS. Color coding: Carbon grey, Hydrogen white, Oxygen red, Fluorine blue, Sulfur yellow.

The highest temperature of the ramp is chosen to correspond to temperature reachable in sonolysis experiments where cavitation bubbles are able to reach such high temperature locally [dSHK+23].

2 Molecular Dynamics simulations

Molecular Dynamics is a simulation method that describes the behavior of an N-body system. It considers each of the N species in the simulation as distinct objects subject to Newtonian mechanics, i.e., with a defined position and velocity dependent only on the forces exerted on them, according to the following equation:

$$m_i \frac{d^2\vec{r}_i(t)}{dt^2} = \vec{f}_i(t), \quad \text{with} \quad \vec{f}_i(t) = -\frac{\partial V(\vec{r}_1(t), \vec{r}_2(t), ..., \vec{r}_n(t))}{\partial \vec{r}_i(t)} \tag{1}$$

Where $\vec{r}_i(t)$ is the position of atom i at time t, m_i is its mass, and $\vec{f}_i(t)$ are the forces applied to atom i at time t. $V = V(\vec{r}_1, \vec{r}_2, ..., \vec{r}_n)$ is the interaction potential among all species.

These forces exerted on each atom then determine its position and velocity at the next timestep through discrete time integration. By repeating this method as many times as necessary, it becomes possible to determine the behavior of atom assembly.

To correctly simulate the behavior of these systems, we need to know the initial configuration, preferably matching, at best, experimental situations. The forces between atoms are derived from the interaction potential $V(\vec{r}_1(t), \vec{r}_2(t), ..., \vec{r}_n(t))$. There are various categories of potentials. *Ab initio* potentials are based on quantum mechanics equations which require significant computational power. There is also a category of semi-empirical potentials that approximate these forces, allowing much shorter computation times for the same simulation. One of the most relevant is the reaxFF one, which is both reactive (allows bond breaking and formation based on bond order concept) and includes variable charges (atomic fractional charges calculated and equilibrated every chosen timestep interval) [SHI+16].

ReaxFF was originally developed to simulate hydrocarbons [vDDLA01] and has undergone numerous evolutions applying it to a broader range of simulations, including oxidation in aqueous environments [YNS+14, BAB+21]. This potential considers numerous factors when calculating the energy contribution of the interaction between each atom in the system. The system's energy is calculated as follows:

$$E_{system} = E_{bond} + E_{over} + E_{under} + E_{val} + E_{pen} + E_{tors} + E_{conj} + E_{vdW} + E_{Coulomb}$$

E_{bond} uses the distance between two atoms to determine the bond order and calculate its energy. The terms E_{over} and E_{under} impose energy penalties when an atom has too many or too few bonds with its neighbors. Additionally, E_{val} and E_{tors} add an energy penalty to the system when the valence and torsion angles deviate from the expected equilibrium value, respectively. E_{pen} is present to penalize certain configurations when two double bonds share the same atom. The term E_{conj} is used to account for conjugated systems, while E_{vdW} represents the van der Waals interaction between different atoms. Finally, $E_{Coulomb}$ represents the Coulomb interactions between atoms due to the partial charges assigned to them by the "Electronegativity Equalization Method" [MGS86, JTB+97].

For completeness, we used the reaxFF parameters used in [SSNA+13, dSHK+23] which were already tested for describing C-F bonds in various situations, including PFAS.

To study the degradation products of PFAS, a methodology similar to Brault *et al.* [BAB+21] was adopted. The simulation boxes are cubes with sides of 15.3 Å containing, randomly located, a PFAS molecule, 10 $HO^\bullet$ radicals, and 30 water molecules. The 10 $HO^\bullet$ radicals allow a concentration relative to the pollutant similar to that found in water when subjected to a plasma discharge on the surface. While 100 water molecules would be needed to represent the correct water density, only 30 were used to make the calculations faster, without influencing the results [BBM+23]. This is a very high ratio of PFAS and $HO^\bullet$ with water molecules:

water molecules are introduced for mimicking the environment of the degradation reactions. This allows accelerating the dynamics for determining the created products. Periodic boundary conditions are applied in all directions, mimicking bulk water processes.

For each considered PFAS, a set of 10 simulations was performed, with different initial conditions and then subjected to equilibration at 300 K for 1000 fs with timesteps of 0.1 fs, followed by a temperature ramp from 300 K to 5300 K with a rate of 50 fs.K^{-1}, ending with a second equilibration step at a constant temperature of 5300 K. The temperature is controlled using a Nose-Hoover thermostat with a 100 fs damping time. We then monitor the evolution of the chemical species present during the simulation for each simulation boxes and then results are averaged. An alternative way was tested: the use of a stepped temperature ramp to give more chance to potential species that might not have time to form in the previous case. However, as seen in Figure 2, there is no noticeable differences. The continuous ramp method was thus retained to easily link integration timesteps to temperature.

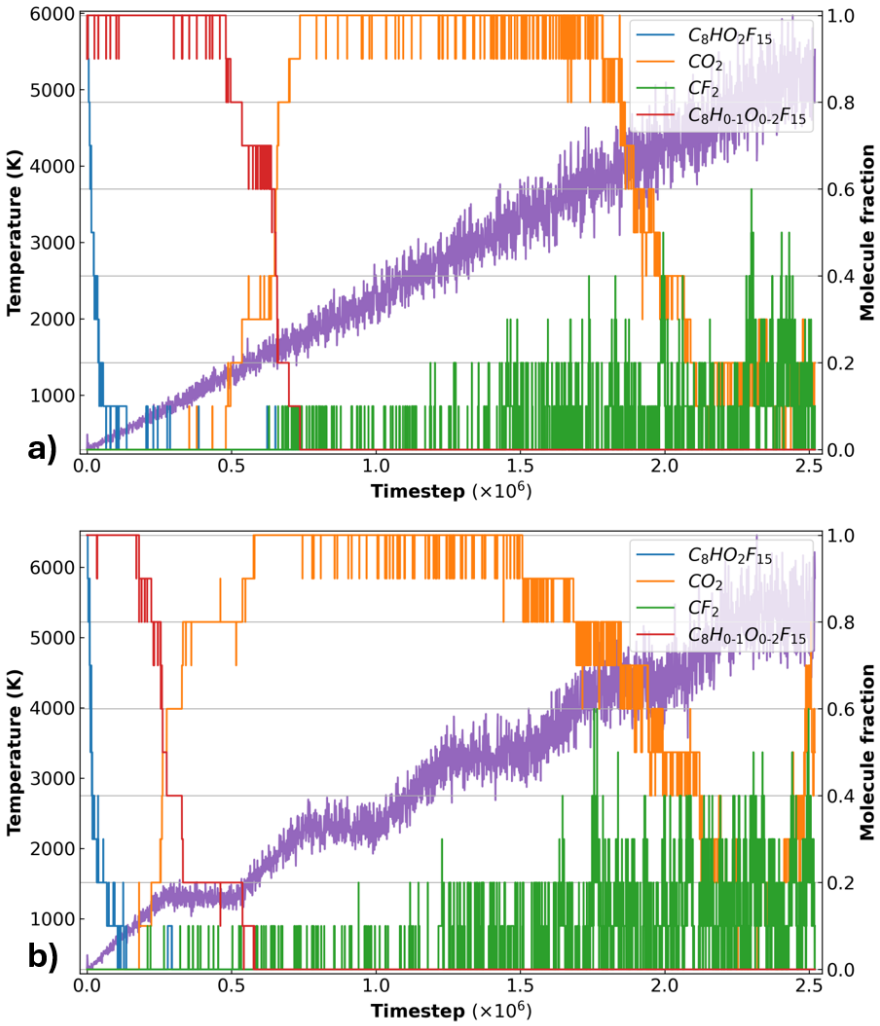

Figure 2: Comparison of a simulation a) without and b) with stepped temperature ramp. In purple is the temperature. The other colors represent the average number of molecules of each species during the simulation. In blue is the original PFOA molecule, in yellow CO_2, in green CF_2, and in red the sum of molecules with 8 carbons and 15 fluorine atoms. We can see that the two figures are quite similar, with reactions occurring faster in terms of time for the stepped ramp but at similar temperatures.

3 Results and discussion

We are interested in the evolution of species during the simulation to determine the reactions that occurred for a PFOA molecule. We average the results over the ten simulations performed to better represent the evolution of various species. Figure 3 shows the reaction path taken at the beginning of the simulation. The blue line represents PFOA; we see that this molecule rapidly disappears in favor of $C_8F_{15}O_2$ (in green), indicating that the hydrogen atom of the functional group of the PFAS molecule is rapidly removed. The next step is much slower and occurs between 900 K ($\approx 3.\ 10^5$ timesteps) and 1700 K ($\approx 6.\ 10^5$ timesteps): $C_8F_{15}O_2$ molecule disappears while a CO_2 molecule (in purple) and a C_7F_{15} molecule (in red) appear, suggesting that the previous molecule splits. Additionally, the yellow curve closely following the green curve shows that no other molecule containing 8 carbon and 15 fluorine atoms is formed.

In the long term, our main molecule continues to degrade. We can see in Figure 4 the continuation of the reaction. Thus, the C_7F_{15} molecules (still in red) are degraded into C_5F_{11} molecules (blue) and C_2F_4 molecules (green), in the temperature range from 2500-3000 K. The C_5F_{11} molecules are then rapidly degraded into C_3F_7 molecules (yellow) and also to C_2F_4 molecules. Then, the C_3F_7 molecules are degraded into C_2F_4 and CF_3 (purple). Finally, the C_2F_4 molecules begin to degrade into two CF_2 molecules around 3400 K. All generated molecules during the 10 runs are listed in Table S1 in the supplementary information.

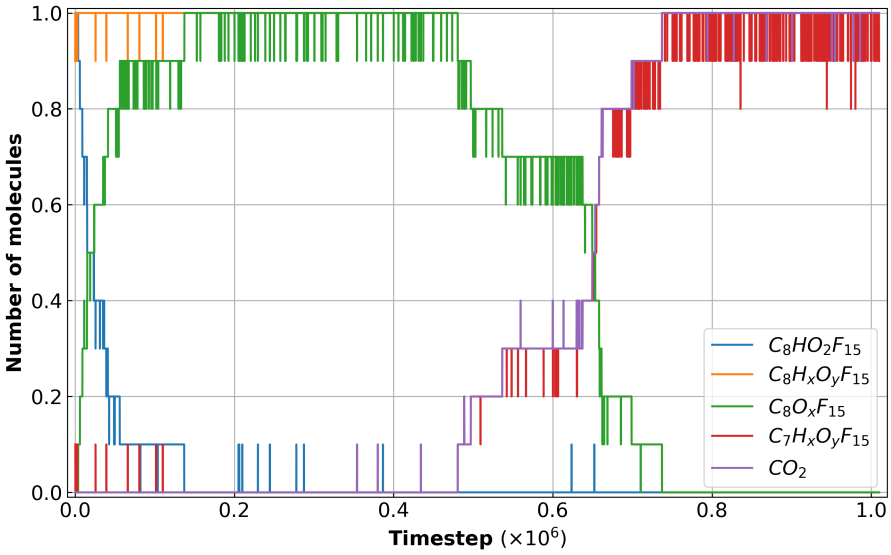

Figure 3: Evolution of the average number of molecules of certain species at the beginning of the simulation. Table S2 in supplementary information gives the details of the considered molecules.

To go further, we identify the products at the end of the reaction in Figure 5. We thus follow the evolution of the number of molecules containing one carbon, an arbitrary number of oxygen and hydrogen, with 4, 3, and 2 fluorine atoms in red, green, and yellow, respectively. The number of $CH_xF_3O_y$ molecules is quite stable from 3500 K, while the number of $CH_xF_2O_y$ continues to increase until 4300 K due to the degradation of $C_2H_xF_4O_y$ molecules seen previously. In the end, we have about 0.2 $CH_xF_4O_y$, 1.2 $CH_xF_3O_y$, 4 $CH_xF_2O_y$. We have represented the sum of molecules containing one carbon and at least one fluorine in blue, and we find the expected 6.4 molecules. Additionally, the number of CO molecules being 1.6, we can be certain of having identified all the degradation products containing carbon found at the end of the simulation. It is worth noting that identifying CF_4 as a relatively rare degradation product demonstrates the utility of our method

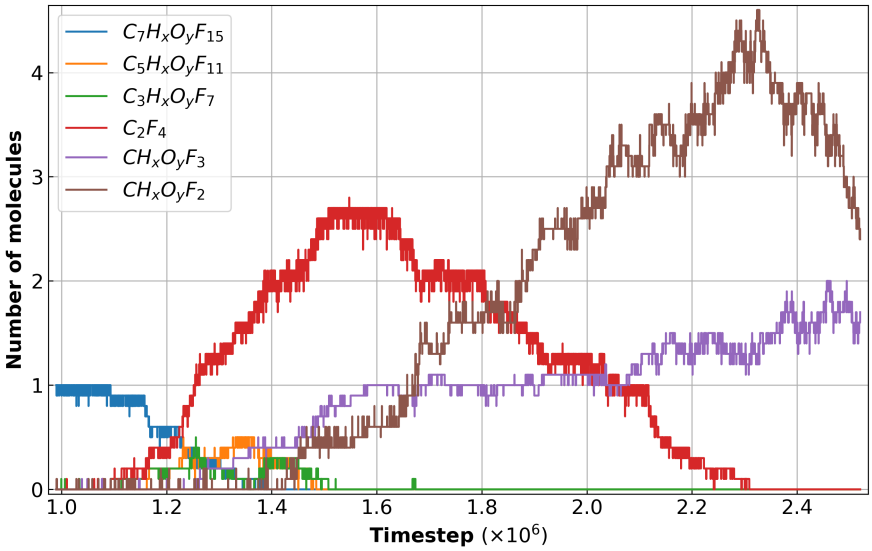

Figure 4: Evolution of the average number of molecules of certain species in the middle of the simulation. Table S3 in supplementary information gives the details of the considered molecules.

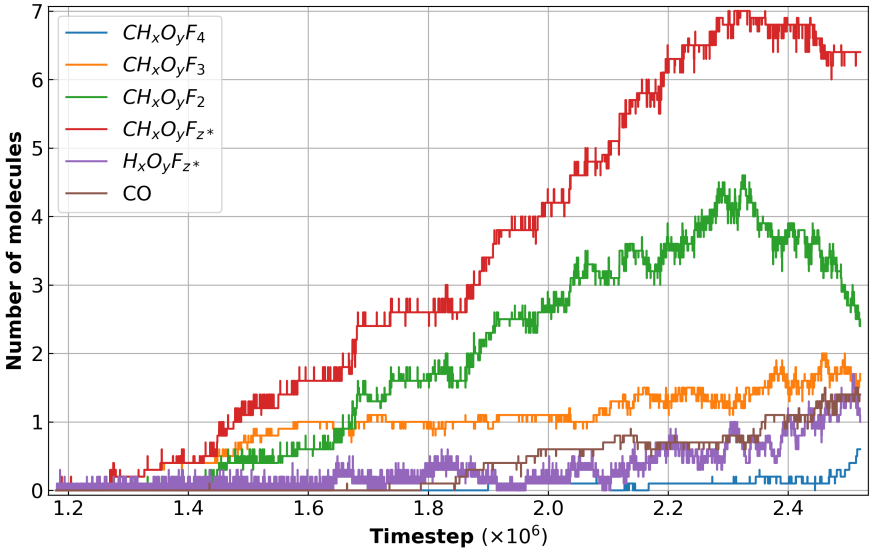

Figure 5: Evolution of the average number of molecules of C1 species at the end of the simulation. x, y = 0, 1, ... and * means z $\geq$ 1. Table S4 in supplementary information gives the details of the considered molecules.

for detecting reactions with a relatively low probability, allowing us to provide a more complete picture of the final and intermediate products that appear during the degradation reaction.

We were able to identify the degradation pathway of a PFOA molecule. Indeed, the molecule first loses its hydrogen, followed by a carbon and two oxygen atoms that form a CO_2. Then, the remaining organic chain is cut two carbons at a time, forming numerous C_2F_4 molecules, which are then mainly degraded into CF_2.

We can represent the reaction sequence as follows:

$$\begin{aligned}
C_8HF_{15}O_2 + HO^\bullet &\longrightarrow C_8F_{15}O_2 + H_2O \\
C_8F_{15}O_2 &\xrightarrow{nHO^\bullet} C_7H_xO_yF_{15} + CO_2 \\
C_7F_{15} &\xrightarrow{nHO^\bullet} C_5H_xO_yF_{11} + C_2F_4 \\
C_5F_{11} &\xrightarrow{nHO^\bullet} C_3H_xO_yF_7 + C_2F_4 \\
C_3F_7 &\xrightarrow{nHO^\bullet} CH_xO_yF_3 + C_2F_4 \\
C_2F_4 &\xrightarrow{nHO^\bullet} 2CF_2 \\
x, y = 0, 1, ...; n &= 0, 1, ...
\end{aligned}$$

This reaction pathways are consistent with literature [LSC+22]. Nevertheless, it should be noticed that the formation of C_7F_{15} can be alternatively followed by the formation of $C_6F_{15}COOH$. This way the carboxylic group always remains up to the triflic acid final product CF_3COOH after interaction with two additional $HO^\bullet$ radicals, H_2O and HF [SFB+19]. It thus requires a higher concentration of $HO^\bullet$ radicals close to the PFOA and related products.

3.1 Case of PFOS

The same methodology can be used for perfluorooctanesulfonic acid (PFOS) with the chemical formula $C_8F_{17}SO_3H$. We find that the molecule also very quickly loses its hydrogen with a HO molecule to form a water molecule. Then, the molecule separates into two new molecules at a temperature ranging from 1700 K to 2300 K. SO_3 and C_8F_{17} molecules are thus formed. The C_8F_{17} molecule will then yield twice a molecule of C_2H_4 when the temperature ranges from 2500 K to 3300 K. The resulting C_4F_9 molecule is then degraded into three different molecules: C_2F_4, CF_2, and CF_3 from 3100 K. At the end of the simulation, SO_3 (sometimes accompanied by one or two water molecules) and numerous CF and CF_2 are obtained. All generated molecules during the 10 runs are listed as Table S5 in the suplementary information.

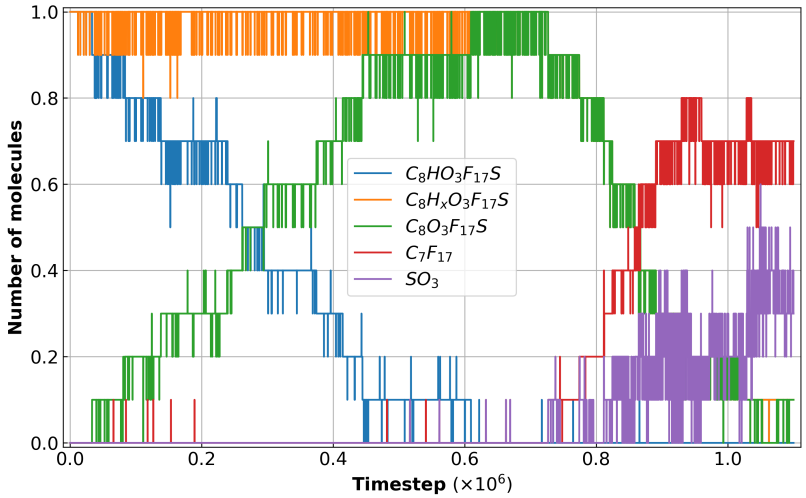

Figure 6: Evolution of the average number of PFOS and product molecules at the beginning of the simulation, up to 0.1 ns. Table S6 in supplementary information gives the details of the considered molecules.

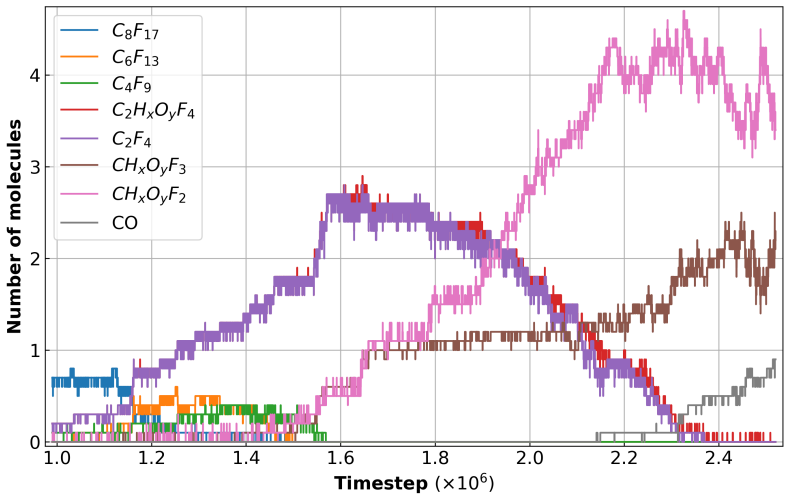

Figure 7: Evolution of the average number of product molecules between 0.1 and 0.25 ns of the simulation. Table S7 in supplementary information gives the details of the considered molecules.

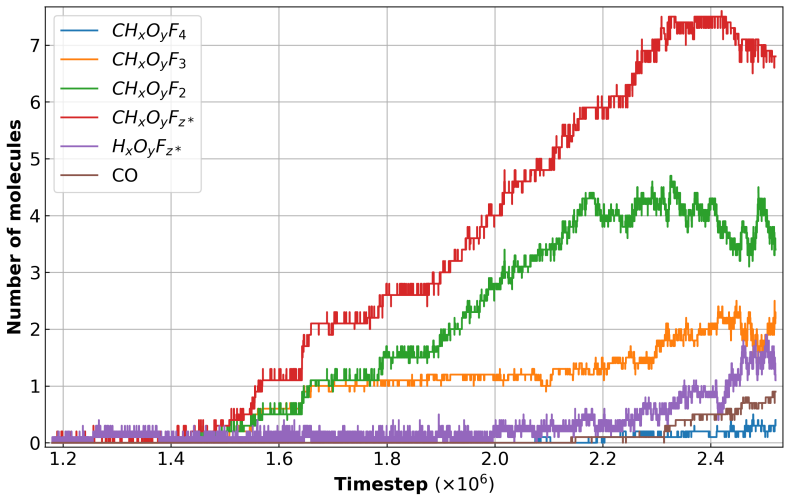

Figure 8: Evolution of the average number of molecules of C1 species at the end of the simulation. x, y = 0, 1, ... and * means z $\geq$ 1. Table S8 in supplementary information gives the details of the considered molecules.

Thus, the reaction pathways extracted from figures 6,7 and 8, consistent with previous experimental findings [LSC+22], can be written as follows:

$$
\begin{aligned}
C_8HF_{17}O_3S + HO^\bullet &\longrightarrow C_8F_{17}O_3S + H_2O \\
C_8F_{17}O_3S &\xrightarrow{nHO^\bullet} C_8H_xO_yF_{17} + SO_3 \\
C_8F_{17} &\xrightarrow{nHO^\bullet} C_6F_{13} + C_2F_4 \\
C_6F_{13} &\xrightarrow{nHO^\bullet} C_3H_xO_yF_7 + C_2F_4 \\
C_4F_9 &\xrightarrow{nHO^\bullet} CH_xO_yF + CH_xO_yF_2 + C_2H_xO_yF_4 \\
x, y &= 0, 1, ...; n = 0, 1, ...
\end{aligned}
$$

Since these simulations have been carried out only with $HO^\bullet$, it should be noticed that under other physicochemical degradation conditions, including other reactive radicals, accessible by reactive Molecular Dynamics simulation, the degradation products, reaction paths, rates of appearance and proportions of metabolites produced over time can be very different, for the same starting PFAS. More generally, this makes it possible to consider describing, by this type of simulation, any advanced oxidation/reduction process, including photo-assisted.

4 Conclusion

This work allowed us to use a relevant ReaxFF potential for simulating the degradation of PFAS in water by HO radical oxidation, which is expected to mimick the effects of plasma interaction with PFAS polluted water. It also validates the simulation methodology involving a temperature ramp during the simulation. This methology allows thus to predict all possible degradation products of PFAS interacting with $HO^\bullet$ in water. Moreover the link between products and temperature can be useful for reverse analysis: knowing the temperature at which a product is formed can be used to infer the best process to obtain it.

Acknowledgments

Conseil Régional Centre Val de Loire is gratefully ackowledged for project Perturb'Eau under grant #2021-00144786.

References

[eud20] Directive (EU) 2020/2184 of the European Parliament and of the Council of 16 December 2020 on the quality of water intended for human consumption , 2020, Last access: 2025-04-30. Available at https://eur-lex.europa.eu/eli/dir/2020/2184/oj.

[AGGH+24] D. Ackerman Grunfeld, D. Gilbert, J. Hou, A. M. Jones, M. J. Lee, T. C. Kibbey, and D. M. O'Carroll, Underestimated burden of per-and polyfluoroalkyl substances in global surface waters and groundwaters, *Nature Geoscience* **17** no. 4 (2024), 340–346. doi:10.1038/s41561-024-01402-8.

[AISH23] R. Amen, A. Ibrahim, W. Shafqat, and E. B. Hassan, A critical review on PFAS removal from water: Removal mechanism and future challenges, *Sustainability* **15** no. 23 (2023), 16173. doi:10.3390/su152316173.

[AOG24] A. Ayodele and E. Obeng-Gyasi, Exploring the potential link between PFAS exposure and endometrial cancer: A review of environmental and sociodemographic factors, *Cancers* **16** no. 5 (2024). doi:10.3390/cancers16050983.

[BAB+21] P. Brault, M. Abraham, A. Bensebaa, O. Aubry, D. Hong, H. Rabat, and M. Magureanu, Insight into plasma degradation of paracetamol in water using a reactive molecular dynamics approach, *Journal of Applied Physics* **129** no. 18 (2021). doi:10.1063/5.0043944.

[BBM+23] P. Brault, F. Bilea, M. Magureanu, C. Bradu, O. Aubry, H. Rabat, and D. Hong, Plasma degradation of water organic pollutants: Ab initio molecular dynamics simulations and experiments, *Plasma Processes and Polymers* **20** no. 11 (2023), e2300116. doi:10.1002/ppap.202300116.

[BAK+23] H. Brunn, G. Arnold, W. Körner, G. Rippen, K. G. Steinhäuser, and I. Valentin, PFAS: forever chemicals—persistent, bioaccumulative and mobile. Reviewing the status and the need for their phase out and remediation of contaminated sites, *Environmental Sciences Europe* **35** no. 1 (2023), 1–50. doi:10.1186/s12302-023-00721-8.

[CYM+23] N. J. Cohen, M. Yao, V. Midya, S. India-Aldana, T. Mouzica, S. S. Andra, S. Narasimhan, A. K. Meher, M. Arora, J. K. Y. Chan, S.-Y. Chan, S. L. Loy, L. Minguez-Alarcon, Y. Oulhote, J. Huang, and D. Valvi, Exposure to perfluoroalkyl substances and women's fertility outcomes in a Singaporean population-based preconception cohort, *Science of The Total Environment* **873** (2023), 162267. doi:10.1016/j.scitotenv.2023.162267.

[vDDLA01] A. C. T. van Duin, S. Dasgupta, F. Lorant, and W. A. Goddard, ReaxFF: A Reactive Force Field for Hydrocarbons, *The Journal of Physical Chemistry A* **105** no. 41 (2001), 9396–9409. doi:10.1021/jp004368u.

[JTB+97] G. O. Janssens, H. Toufar, B. G. Baekelandt, W. J. Mortier, and R. A. Schoonheydt, The electronegativity equalization method (EEM) as a promising tool for the analysis of zeolite catalyzed reactions, in *Studies in Surface Science and Catalysis*, **105**, Elsevier, 1997, pp. 725–732. doi:10.1016/S0167-2991(97)80622-2.

[LVG10] Y. Lee and U. Von Gunten, Oxidative transformation of micropollutants during municipal wastewater treatment: Comparison of kinetic aspects of selective (chlorine, chlorine dioxide, ferratevi, and ozone) and non-selective oxidants (hydroxyl radical), *Water research* **44** no. 2 (2010), 555–566. doi:10.1016/j.watres.2009.11.045.

[LSC+22] S. C. E. Leung, P. Shukla, D. Chen, E. Eftekhari, H. An, F. Zare, N. Ghasemi, D. Zhang, N.-T. Nguyen, and Q. Li, Emerging technologies for PFOS/PFOA degradation and removal: A review, *Science of The Total Environment* **827** (2022), 153669. doi:10.1016/j.scitotenv.2022.153669.

[MGS86] W. J. Mortier, S. K. Ghosh, and S. Shankar, Electronegativity-equalization method for the calculation of atomic charges in molecules, *Journal of the American Chemical Society* **108** no. 15 (1986), 4315–4320. doi:10.1021/ja00275a013.

[SHI+16] T. P. Senftle, S. Hong, M. M. Islam, S. B. Kylasa, Y. Zheng, Y. K. Shin, C. Junkermeier, R. Engel-Herbert, M. J. Janik, H. M. Aktulga, T. Verstraelen, A. Grama, and A. C. T. van Duin, The ReaxFF reactive force-field: development, applications and future directions, *npj computational* **2** no. 1 (2016), 15011. doi:10.1038/npjcompumats.2015.11.

[SFB+19] R. K. Singh, S. Fernando, S. F. Baygi, N. Multari, S. M. Thagard, and T. M. Holsen, Breakdown products from perfluorinated alkyl substances (PFAS) degradation in a plasma-based water treatment process, *Environmental science & technology* **53** no. 5 (2019), 2731–2738. doi:10.1021/acs.est.8b07031.

[SSNA+13] S. K. Singh, S. G. Srinivasan, M. Neek-Amal, S. Costamagna, A. C. Van Duin, and F. Peeters, Thermal properties of fluorinated graphene, *Physical Review B—Condensed Matter and Materials Physics* **87** no. 10 (2013), 104114. doi:10.1103/PhysRevB.87.104114.

[dSHK+23] B. B. de Souza, S. A. Hewage, J. A. Kewalramani, A. C. van Duin, and J. N. Meegoda, A ReaxFF-based molecular dynamics study of the destruction of PFAS due to ultrasound, *Environmental Pollution* **333** (2023), 122026. doi:10.1016/j.envpol.2023.122026.

[WX12] J. L. Wang and L. J. Xu, Advanced oxidation processes for wastewater treatment: formation of hydroxyl radical and application, *Critical reviews in environmental science and technology* **42** no. 3 (2012), 251–325. doi:10.1080/10643389.2010.507698.

[YNS+14] M. Yusupov, E. C. Neyts, P. Simon, G. Berdiyorov, R. Snoeckx, A. C. T. van Duin, and A. Bogaerts, Reactive molecular dynamics simulations of oxygen species in a liquid water layer of interest for plasma medicine, *Journal of Physics D: Applied Physics* **47** no. 2 (2014), 025205. doi:10.1088/0022-3727/47/2/025205.